

A discrete geometric approach for simulating the dynamics of thin viscous threads

B. Audoly^{a,*}, N. Clauvelin^{a,b}, P.-T. Brun^{a,c}, M. Bergou^{d,e}, E. Grinspun^d,
M. Wardetzky^f

^a*Institut Jean Le Rond d'Alembert, UMR 7190, UPMC Univ. Paris 06 and CNRS,
F-75005 Paris, France*

^b*BioMaPS Institute, Rutgers, the State University of New Jersey, Piscataway, NJ, USA*

^c*Laboratoire FAST, UPMC Univ. Paris 06, Université Paris-Sud and CNRS, Bâtiment
502, Campus Universitaire, Orsay 91405, France*

^d*Computer Science, Columbia University, New York, NY, USA*

^e*Adobe Systems Incorporated*

^f*Institute for Numerical and Applied Mathematics, University of Göttingen, 37083
Göttingen, Germany*

Abstract

We present a numerical model for the dynamics of thin viscous threads based on a discrete, Lagrangian formulation of the smooth equations. The model makes use of a condensed set of coordinates, called the centerline/spin representation: the kinematical constraints linking the centerline's tangent to the orientation of the material frame is used to eliminate two out of three degrees of freedom associated with rotations. Based on a description of twist inspired from discrete differential geometry and from variational principles, we build a full-fledged discrete viscous thread model, which includes in particular a discrete representation of the internal viscous stress. Consistency of the discrete model with the classical, smooth equations is established formally in the limit of a vanishing discretization length. The discrete models lends itself naturally to numerical implementation. Our numerical method is validated against reference solutions for steady coiling. The method makes it possible to simulate the unsteady behavior of thin viscous jets in a robust and efficient way, including the combined effects of inertia, stretching, bending, twisting, large rotations and surface tension.

Keywords: viscous rod, bending, twisting, Rayleigh-Taylor analogy, viscous coiling

*Corresponding author

1. Introduction

1.1. Context

The flow of thin viscous filaments is relevant to a variety of industrial processes such as the drawing and spinning of polymer and glass fibers [1, 2, 3], and to natural phenomena such as formation of Pele’s hair by lava ejected at high speed by volcanoes [4]. In art, Jackson Pollock took advantage of the coiling instability of a thin viscous fluid, the paint, impinging a surface, the canvas, to produce a variety of decorative patterns by a fluid-mechanical process [5]. A commonplace version of the same coiling instability is observed when a thin thread of honey is poured on a morning’s toast. This steady coiling problem is prototypical of the dynamics of thin threads. Its apparent simplicity has made it appealing to fluid mechanicians for a long time [6, 7]; however the various regimes of steady coiling and its non-linear features, such as multistability, have been understood in full details only recently [8, 9, 10, 11]. To a large extent, the analysis of steady coiling has been made possible by the availability of numerical simulation: the shape of the thread in the co-rotating frame is stationary, and is given by a non-linear boundary-value problem [9] which has been solved using numerical continuation.

In this paper we are interested in the simulation of the unsteady behavior of thin threads, which is far less advanced. As an illustration, consider a recently proposed variant of the coiling problem, similar to Pollock’s painting technique, whereby the target surface moves horizontally at a constant velocity. The relative motion suppresses steady coiling solutions and forces the flow to become unsteady. More than ten different patterns can be produced by varying the lateral velocity of the surface and the fall height [12, 13], a number of which have convoluted and intriguing shapes. The patterns are reminiscent of stitch patterns, and the experiment has been coined the ‘fluid-mechanical sewing machine’. This experiment nicely illustrates the complex behavior that can result from the dynamics of a thin, perfectly viscous filament. Existing numerical methods are unable to reproduce this behavior, even though the principle of the experiment is simple. This highlights the need for a robust and efficient method for simulating the dynamics of thin viscous threads.

The dynamics of thin viscous threads is governed by the interplay of three local modes of deformation, namely stretching, bending and twisting modes [14, 15]. At the global scale, these modes are coupled by geometrically non-linear terms accounting for finite rotations. This coupling makes the resulting dynamics remarkably rich. Another, unfortunate consequence of the nonlinearity is the absence of analytical solutions to the dynamical equations. This makes the development of robust simulation methods even more desirable. The main difficulty in developing such a method is that the underlying equations are numerically stiff, as the governing equations are non-linear partial differential equations of fourth order in space. This paper tackles this difficulty by introducing a careful and well-controlled space discretization. In fact, we introduce a full-fledged *discrete* viscous thread model by extending all the relevant physical quantities, such as strain rates and internal stress, to the discrete setting.

Fluid mechanical problems involving free boundary conditions can be simulated using refined variants of the marker and cells method, namely the method of [16, 17] for 2d viscous flows, and the GENSMAC method [18, 19] for 3d viscous flows; more recently implicit schemes coupled with projection methods have been proposed, see e. g. [20]. The present paper is concerned with thin filaments, for which the above methods are not efficient: when the thickness is small compared to the longitudinal length scale, it is beneficial to use dimensionally reduced equations as a starting point for simulations. Thanks to dimensional reduction, the structure of the flow at small scale is solved analytically, which makes it possible to use a simulation grid much coarser than the thickness.

While our simulation method addresses the general non-steady dynamics of a thin thread governed by the combined effects of twist, bending and stretching forces, inertia and large rotations, a number of particular cases have been simulated in the literature. Steadily rotating viscous threads are described by time-independent equations in the co-rotating frame, which have been solved numerically using methods for two-point boundary value problems [9, 11, 21]. The dynamics of a viscous string, where both the bending and twisting modes are neglected, has been considered [22]. The periodic folding of a viscous thread or sheet has been considered in a 2d geometry [23, 24] where twist does not play any role. By combining the simulation of steady solutions with analytical expansions describing oscillatory perturbations of small amplitude, the stability of both the steady coiling solution [11] and of the catenary-like profile of a dragged thread [25] have been calculated. Many other problems, such as the existence of rotatory folding, the competition between folding and coiling [26], the stitch patterns produced by the fluid-mechanical sewing machine [12] and the destabilization of steady coiling by precession [27] remain inaccessible to those simulation methods that are based on restrictive assumptions.

In comparison to viscous threads, elastic rods have received a lot of attention, both from the perspective of analysis [28, 29, 30, 31] and simulation [32, 33, 34, 35, 36, 37]. By the Rayleigh-Taylor analogy [7], the stress in a viscous fluid is identical the stress in an elastic solid having the same geometry, when the strain *rate* relevant to the viscous case is replaced with the *current* strain relevant to the elastic case. Stated differently, the main difference between the elastic and viscous problems is the presence of an additional time derivative in the right-hand side of the viscous constitutive laws. This analogy explains the buckling of viscous sheets [38, 39], a phenomenon usually associated with elastic structures. One can take advantage of this analogy to simulate the dynamics of viscous threads using a simulation tool written for elastic rods [40]; we explored this approach in a conference paper [41]. The possibility to recycle an existing elastic code for viscous simulations with minimal additional work is very attractive. However, the initial effort associated with implementing and validating an elastic code is high. In situations where no elastic code is available, it is simpler to implement a viscous simulator directly. In the present paper we follow this approach and propose a numerical method that does not rely on an external library for solving the dynamics of elastic rods.

While thin elastic rods are usually considered inextensible, the stretching

mode has to be retained in viscous threads, in addition to the usual bending and twisting modes. In both the elastic and viscous cases, dimensional analysis shows that the strain, or strain rate, associated with the stretching mode is small compared to that associated with the bending and twisting modes, as the corresponding modulus is larger by a factor proportional to the inverse of the small aspect-ratio squared, a very large number. A specificity of the viscous case is that the stretching mode cannot be neglected, even though its strain rate is small. This is well illustrated by the phenomenon of helical coiling: a thin thread poured from a container onto a fixed obstacle gets stretched by gravity and remains straight over almost the entire fall height, but it bends and twist severely in a small boundary layer near the bottom. Even though the stretching is very mild, its effect is cumulated over the entire time of descent, unlike the bending and twisting modes that come into play only near the surface. For this reason, the stretching mode has to be considered in simulations of viscous threads. By the incompressibility condition, variations of the thread's radius along its centerline need be considered as well. Another difference with the elastic case is that capillary forces can have a strong effect on the motion, and must be taken into account.

1.2. Model

The derivation of dimensionally reduced models for thin viscous filaments has a long history and is still a research topic. The equations for thin viscous threads were derived by asymptotic expansion from the equations for a 3d viscous fluids by Entov and Yarin [42]. Their work builds upon the previous analyses of viscous stretching by Trouton [14], and of viscous bending by Buckmaster and co-workers [43, 44]. In the case of elliptical cross-sections, the dynamics of the centerline and the evolution of the geometry of the cross-section are coupled; the corresponding equations have been derived by dimensional reduction in 1d by Dewynne and collaborators [45], and later extended to a capillary fluid by [46]. Recent derivations of the equations for thin threads benefit from a clear identification of the mechanical quantities in the 1d model [47], and of the systematic use of Lagrangian coordinates [21]. Asymptotic models accounting for more general constitutive laws have been proposed: the case of a visco-elastic fluid is treated in [48], and a general framework is considered in [49] which can produce a variety of asymptotic models when a specific set of physical effects is considered.

Here we consider the dynamics of a thin filament of an incompressible, purely viscous fluid having circular cross-section, under the action of external forces such as gravity, and internal forces (viscous stretching, bending, twisting, and capillary tension). We consider the 3d problem, and the curvature and kinematical twist of the thread can be comparable to, or smaller than the inverse of the thread's length. Even though the fluid is very viscous, the effect of inertia is considered. The role of inertia is well illustrated by the classical analysis of the pendulum modes of a viscous string, see e. g. [10]: in this almost straight geometry, the flow in the axial direction is typically governed by a small Reynolds

number and dominated by viscosity, although the flow in the transverse direction, which is characterized by different length and time scales, is associated with a much larger Reynolds number and dominated by inertia. In the general case, the local axial and transverse modes get coupled by the curvature of the filament. For this reason, we retain the inertial term in the balance of momentum even though the constitutive laws are dominated by viscosity (Stokes' fluid).

We assume that the cross-section of the filament is a disk, and remains so as the filament deforms. Even when a viscous filament is extruded from a non-circular opening, surface tension tends to round off the shape of the cross-sections; this happens over a time scale which we assume is short compared that of the flow. This is not always the case, and the possibility to account for non-axisymmetric cross-sections has been demonstrated in the elastic case using our numerical method [35, 41]. While the general case raises no fundamental difficulty, our presentation is limited to the case of axisymmetric cross-sections, which is simpler: all the directions in the cross-sections are then equivalent and there is no need to keep track of their absolute orientations. The case of tubes, i. e. of non simply-connected cross-sections [50], is not considered here but this extension may be considered in future work as well.

1.3. Proposed approach

The main features of our numerical method are the following. It is based on a 1d model obtained by dimensional reduction, which makes it much more efficient than a general-purpose model for 3d viscous flows. We use a Lagrangian grid, making simulation vertices flow along with the fluid; this simplifies the computation of viscous forces which, by the constitutive law, are proportional to the comoving time derivative of the kinematical twist and curvature. We use a reduced set of coordinates and eliminate two out of three degrees of freedom associated with rotations, by making use of the fact that cross-sections initially perpendicular to the centerline remain so during motion: rotations are represented using a single degree of freedom. In addition, the absolute angle of twist of the cross-sections is eliminated from the equations, using the fact that the cross-sections are circular. This results in an effective description of rotations which only makes use of the instantaneous angular twist velocity, denoted v . Internal viscous forces include the three physically relevant contributions of stretching, bending and twisting. The discrete expression of these forces is derived based on a Rayleigh potential using variational methods. This leads naturally to discrete viscous forces. The Rayleigh potential plays a similar role in the viscous setting as the elastic energy in the elastic setting. The viscous forces are computed in a linear implicit manner, which means that the expression for the viscous forces is extrapolated to their value at the end of the time step, based on a linearization carried out at the beginning of the time step. This provides a good compromise between stability and ease of implementation. A fully implicit evaluation of these forces is also possible, as discussed in section 9.3.

Our main contribution is to propose an elaborate space discretization of a viscous thread by considering a fully discrete model. All the relevant physical

quantities, such as the strain rates and the viscous forces, are defined in the discrete setting. In this discrete view, bending is represented by the turning angles of the centerline at the vertices, and we do not need to assume that the turning angles remain small at all times. As a consequence, the simulation of the discrete model is stable even if the mesh size is comparable to the smallest radius of curvature of the thread. By contrast, stability of a numerical scheme based on an *ad hoc* discretization of the smooth equations usual requires that the grid size is much smaller than the smallest radius of curvature; in practice, this requirement is severe as thin threads tend to spontaneously form strongly curved region near the endpoints (such as the tiny rotating coils at the bottom of a thin thread stretched by gravity and hitting a hard surface). The ability to run simulations with a relatively coarse mesh is an important advantage of the discrete model, as the maximum time step allowed by Nyquist stability criterion decreases rapidly with mesh size in the presence of fourth-order space derivatives: the simulation of coarser meshes is much more efficient. Given the numerical stiffness of the underlying problem, robustness is a central issue in the simulation of viscous threads. We address this issue by keeping full control of the space discretization.

The discretization of bending in elastic rods is routinely done using flexural springs at hinges [51], and the extension to viscous bending is straightforward. Enforcing the twist forces is much less common. Our discretization of twist is based on a discrete notion of twist, which is directly borrowed from our previous work on elastic rods [35]. This discrete notion of twist is based on concepts from discrete differential geometry, namely the holonomy of a discrete curve. This representation of twist builds upon previous work highlighting the geometrical origin of twist [52, 53, 54], and on related numerical methods used in mechanical engineering [55].

This paper is organized as follows. In section 2 we derive useful identities of geometry and differential calculus. In section 3 the equations for thin viscous threads are formulated in a way that prepares the extension to the discrete the setting, by making use of a Lagrangian description of motion and by deriving the internal viscous forces and moments from variational principles. Section 4 establishes the equivalence with the formulation of the equations for thin threads classically used by fluid mechanicians. In section 5 the discrete model is presented in close analogy with the smooth case of section 3; this section is at the core of the paper. Section 6 considers time discretization; formulae that are required in the implementation are summarized, and we discuss the treatment of boundary conditions and adaptive mesh refinement. In section 7, we consider the coupling of the thread with external bodies, such as a fluid container or hard surface. In section 8, the code is validated against reference solutions for steady coiling. In section 9, we discuss limitations and perspectives.

In this paper, an effort is made to establish the equivalence of different formulations. The formulation of the equation of motion due to Kirchhoff is popular among fluid mechanicians as it has a clear intuitive meaning, while that based on the Rayleigh potential is rarely if ever used in this community but lends itself to a natural discretization. Working out the connection between

these equivalent formulations will hopefully help to make this paper accessible to different communities. In addition, presenting the discrete model in parallel with the smooth model provides mutual insights into them. The reader should keep in mind that only a small fraction of the formulae presented in the paper are required for the purpose of implementing the method. These formulae are recapitulated in section 6.4.

2. Mathematical toolbox

In this section we introduce some notations and mathematical identities relevant to the mechanics of thin viscous threads, such as infinitesimal rotations and the covariant derivative.

2.1. Perpendicular projection

We use underlines for vectors, and double underlines for rank-two tensors (matrices). For any unit vector \underline{q} and for any vector \underline{a} , the projection \underline{P}_\perp in the direction perpendicular to \underline{q} is defined by

$$\underline{P}_\perp(\underline{q}, \underline{a}) = (\underline{1} - \underline{q} \otimes \underline{q}) \cdot \underline{a} = \underline{a} - (\underline{q} \cdot \underline{a}) \underline{q}, \quad (1)$$

where the last term in the right-hand side is the longitudinal projection.

2.2. Infinitesimal rotations

Consider an orthonormal frame $\underline{d}_i(\sigma)$, $i = 1, 2, 3$, which is function of a continuous parameter σ : for any pair of integer indices $1 \leq i, j \leq 3$, and for every σ , we have

$$\underline{d}_i(\sigma) \cdot \underline{d}_j(\sigma) = \delta_{ij}, \quad (2)$$

where δ_{ij} is Kronecker's symbol, equal to 1 if $i = j$ and to 0 otherwise. We shall assume that the frame is \mathcal{C}^1 smooth with respect to the parameter σ .

Infinitesimal rotations can be expressed by means of a skew-symmetric matrix, or equivalently as the multiplication by a vector $\underline{\Gamma}(\sigma)$ using the cross product. More accurately, for any value of the parameter σ , the Darboux vector $\underline{\Gamma}(\sigma)$ is defined as the unique vector such that for any $i = 1, 2, 3$:

$$\frac{d\underline{d}_i(\sigma)}{d\sigma} = \underline{\Gamma}(\sigma) \times \underline{d}_i(\sigma). \quad (3)$$

This definition will be used both when σ is the time t , or the arc length S . This leads to the notions of instantaneous angular velocity $\underline{\Gamma}(t) = \underline{\omega}$, or twist-curvature vector $\underline{\Gamma}(S) = \underline{\pi}$, respectively.

An explicit expression for the Darboux vector can be found by singling out any particular vector \underline{d}_i in the triad, say \underline{d}_3 :

$$\underline{\Gamma}(\sigma) = \underline{d}_3 \times \frac{d\underline{d}_3}{d\sigma} + \underline{\Gamma}_3 \underline{d}_3, \quad (4)$$

where $\Gamma_3 = \underline{\Gamma} \cdot \underline{d}_3$ is defined by

$$\Gamma_3(\sigma) = \frac{d\underline{d}_1(\sigma)}{d\sigma} \cdot \underline{d}_2(\sigma). \quad (5)$$

This can be checked by inserting equation (5) into equation (4) and then into equation (3).

2.3. Covariant derivative

Let us consider an orthonormal triad $\underline{d}_i(\sigma)$ and the associated Darboux vector $\underline{\Gamma}(\sigma)$. For any vector field $\underline{a}(\sigma)$, we define the covariant derivative as

$$\frac{\tilde{d}\underline{a}(\sigma)}{\tilde{d}\sigma} = \frac{d\underline{a}(\sigma)}{d\sigma} - \underline{\Gamma}(\sigma) \times \underline{a}(\sigma). \quad (6)$$

It can be interpreted as the derivative measured in the frame moving with the triad \underline{d}_i . In agreement with this interpretation, we note that equation (3) can be rewritten as

$$\frac{\tilde{d}\underline{d}_i}{\tilde{d}\sigma} = 0. \quad (7)$$

The covariant derivative satisfies the following identities, the proof of which is left to the reader. The general Leibniz rule for the product of a scalar function $f(\sigma)$ by a vector $\underline{a}(\sigma)$ reads

$$\frac{\tilde{d}(f(\sigma) \underline{a}(\sigma))}{\tilde{d}\sigma} = \frac{df(\sigma)}{d\sigma} \underline{a}(\sigma) + f(\sigma) \frac{\tilde{d}\underline{a}(\sigma)}{\tilde{d}\sigma}. \quad (8)$$

In the first term of the right-hand side above, the regular derivative of a scalar function is used. In the case of the scalar product of two vectors we have

$$\frac{d(\underline{a} \cdot \underline{b})}{d\sigma} = \frac{\tilde{d}\underline{a}}{\tilde{d}\sigma} \cdot \underline{b} + \underline{a} \cdot \frac{\tilde{d}\underline{b}}{\tilde{d}\sigma}. \quad (9)$$

In the context of thin viscous threads, an important property of the covariant derivative is its compatibility with the tangent and the normal projections. For any vector \underline{a} we define the tangent and normal projections, using the last triad vector \underline{d}_3 as the tangent direction:

$$\underline{a} = a_3 \underline{d}_3 + \underline{a}^\perp, \quad \text{where } a_3 = \underline{a} \cdot \underline{d}_3 \quad \text{and} \quad \underline{a}^\perp = \underline{P}_\perp(\underline{d}_3, \underline{a}). \quad (10)$$

Here \underline{P}_\perp is the perpendicular projection operator defined in equation (1). A consequence of equations (7–9) is that the covariant derivative lives in the plane orthogonal to \underline{d}_3 if $\underline{a}(\sigma)$ does so for all values of σ , and is aligned with the tangent if $\underline{a}(\sigma)$ is aligned with the tangent for all σ . In other words, both the tangential and normal projections commute with the covariant time derivative,

$$\frac{\tilde{d}\underline{a}}{\tilde{d}\sigma} \cdot \underline{d}_3 = \frac{da_3}{d\sigma}, \quad \left(\frac{\tilde{d}\underline{a}}{\tilde{d}\sigma} \right)^\perp = \frac{\tilde{d}(\underline{a}^\perp)}{\tilde{d}\sigma}. \quad (11)$$

By contrast the regular derivative $d/d\sigma$ does not commute with the projection operators. Note that in the first equation above, we use a regular derivative for the scalar quantity a_3 , hence the absence of a tilde.

3. Smooth setting: a Lagrangian description of viscous threads

The equations for the dynamics of thin viscous threads are usually expressed in Eulerian variables, see for instance references [11]. In the present section we reformulate these equations in Lagrangian variables. This will make it possible to extend the geometrical discretization of twist of Bergou et al. [35], and then to derive a discrete model of viscous threads in a natural way. A Lagrangian formulation of the equations can be found in reference [21] but we are not aware of any numerical method that actually makes use of it; most numerical papers consider steady problems, for which an Eulerian grid is sufficient.

Below, we introduce the smooth quantities that are relevant to the kinematics and dynamics of viscous threads. They are introduced in a way that makes it straightforward to identify their discrete counterparts later on. Since the viscous thread can stretch, we make a careful distinction between the arc length measured in reference configuration, which is denoted S , and the arc length measured in actual configuration, denoted s .

3.1. Reference configuration

Our Lagrangian description requires the definition of a reference configuration. This reference configuration can be imaginary, and does not need to be the configuration of the thread at any particular time. A convenient choice is to define the reference configuration to be an infinite, circular cylinder of constant radius a_0 , as illustrated in figure 1. Obviously the equations of motion will be independent of the choice of the reference configuration, and of the value of the reference radius a_0 in particular.

The fluid is considered incompressible. It therefore simpler, although it is not required strictly speaking, to assume that the mapping between the reference and actual configurations preserves volume. This is what we do in equations (23).

3.2. Kinematics of centerline

Let S be the Lagrangian coordinate, and t the time. For any function $f(S, t)$, we denote its spatial derivative using a prime,

$$f'(S, t) = \frac{\partial f(S, t)}{\partial S}, \quad (12)$$

and its time derivative using a dot,

$$\dot{f}(S, t) = \frac{\partial f(S, t)}{\partial t}. \quad (13)$$

By definition, the Lagrangian coordinate S follows fixed fluid particles. The time derivative introduced above is known as a *convective* derivative, and is often written $\dot{f} = \frac{\partial f}{\partial t} = \frac{Df}{Dt}$ in the Eulerian context.

At time t the centerline of the thread is given by the function $\underline{x}(S, t)$, see figure 1. The material tangent of the thread is denoted $\underline{T}(S, t)$ and defined by

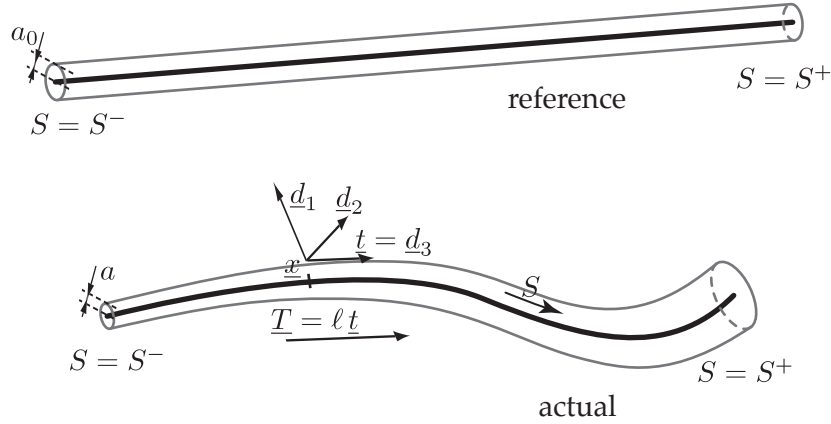


Figure 1: Reference and actual configuration of the thread.

$$\underline{T}(S, t) = \underline{x}'(S, t). \quad (14)$$

Note that this is not a unit vector in general.

The norm of $\underline{T}(S, t)$, denoted $\ell(S, t)$, measures the amount of stretching of the centerline with respect to the reference configuration:

$$\ell(S, t) = |\underline{T}(S, t)| = \left| \frac{\partial \underline{x}(S, t)}{\partial S} \right|. \quad (15)$$

The unit tangent to the centerline is then defined as

$$\underline{t}(S, t) = \frac{\underline{T}(S, t)}{\ell(S, t)}. \quad (16)$$

In our Lagrangian description, the arc length s in actual configuration is viewed as a secondary quantity. It can be reconstructed by integration of the differential equation expressing the identity $ds = |d\underline{x}|$, namely

$$s'(S, t) = \frac{\partial s(S, t)}{\partial S} = \ell(S, t).$$

The Lagrangian axial strain rate d is defined by

$$d(S, t) = \frac{\partial \ell(S, t)}{\partial t}, \quad (17)$$

and measures the rate of stretching per unit time. Note that this quantity differs from the Eulerian strain rate, noted d^E and defined later in equation (65c).

In the Lagrangian framework the velocity \underline{u} is simply the time derivative of position,

$$\underline{u}(S, t) = \frac{\partial \underline{x}(S, t)}{\partial t}, \quad (18)$$

and the acceleration its second time derivative,

$$\underline{\gamma}(S, t) = \frac{\partial \underline{u}(S, t)}{\partial t} = \frac{\partial^2 \underline{x}(S, t)}{\partial t^2}. \quad (19)$$

A kinematical relation between the strain rate $d(S, t)$ and the velocity $\underline{u}(S, t)$ can be established as follows:

$$d(S, t) = \frac{\partial \ell}{\partial t} = \frac{1}{2\ell} \frac{\partial(\ell^2)}{\partial t} = \frac{1}{2\ell} \frac{\partial(\underline{T}^2)}{\partial t} = \frac{1}{\ell} \underline{T} \cdot \frac{\partial \underline{T}}{\partial t} = \underline{t}(S, t) \cdot \frac{\partial \underline{u}(S, t)}{\partial S}. \quad (20)$$

In the last equality, we have used the following identity, coming from the permutation of derivatives with respect of t and S :

$$\frac{\partial \underline{T}}{\partial t} = \frac{\partial}{\partial t} \left(\frac{\partial \underline{x}}{\partial S} \right) = \frac{\partial}{\partial S} \left(\frac{\partial \underline{x}}{\partial t} \right) = \frac{\partial \underline{u}}{\partial S}.$$

Another useful identity follows from inserting the definition of ℓ in equation (16), $\underline{T} = \ell \underline{t}$, into the left-hand side of the equation above. Expanding the time derivative, we find $\ell \underline{\dot{t}} + \underline{t} \dot{\ell} = \underline{u}'(S)$. Applying the perpendicular projection operator $\underline{P}_\perp(\underline{t}, \cdot)$ on both sides and using $\underline{P}_\perp(\underline{t}, \underline{t}) = \underline{0}$ and $\underline{P}_\perp(\underline{t}, \underline{\dot{t}}) = \underline{\dot{t}}$ (the other term cancels since $\underline{t} \cdot \underline{\dot{t}} = \frac{1}{2} \frac{\partial \ell^2}{\partial t} = 0$), we have

$$\frac{\partial \underline{t}(S, t)}{\partial t} = \frac{1}{\ell(S, t)} \underline{P}_\perp \left(\underline{t}(S, t), \frac{\partial \underline{u}(S, t)}{\partial S} \right). \quad (21)$$

This equation yields the time derivative of unit tangent as a function of center-line geometry and of the velocity \underline{u} .

3.3. Incompressibility: radius and related quantities

The viscous fluid is considered incompressible, as explained in section 3.1, and we assume that the mapping from the reference configuration to the actual configuration preserves volume. The reference configuration is a cylinder with a uniform radius a_0 and a cross sectional area $A_0 = \pi a_0^2$. The radius of the thread in the actual configuration is denoted $a(S, t)$, the area is $A(S, t)$, and $I(S, t)$ stands for the moment of inertia. We assume that the thread has locally a cylindrical geometry, in which case

$$A(S, t) = \pi a^2(S, t), \quad I(S, t) = \frac{\pi a^4(S, t)}{4}. \quad (22)$$

The fluid volume enclosed in an infinitesimal length of the thread is $A(S, t) ds = A(S, t) \ell(S, t) dS$ in the actual configuration, and $A_0(S, t) dS$ in reference configuration, see figure 1. As a result, the incompressibility of the fluid is expressed by

$$a(S, t) = \frac{a_0}{\sqrt{\ell(S, t)}}, \quad A(S, t) = \frac{A_0}{\ell(S, t)}, \quad I(S, t) = \frac{I_0}{\ell^2(S, t)} \quad (23)$$

where the subscript naught refers to the reference configuration, for which we have $\ell_0 = 1$ by convention. In particular, the moment of inertia in the reference configuration reads $I_0 = \pi a_0^4/4$.

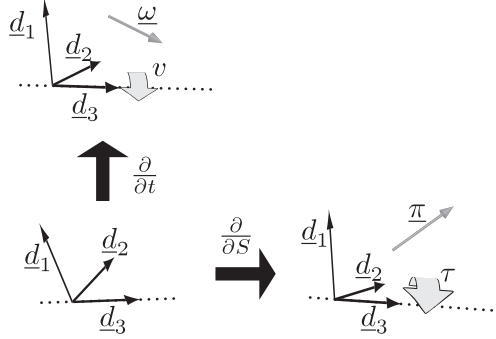


Figure 2: Darboux vectors (infinitesimal rotations) associated with spatial or temporal derivative of the material frame: instantaneous rotation velocity $\underline{\omega}$ and twist-curvature vector $\underline{\pi}$. A compatibility condition for $\underline{\omega}$ and $\underline{\pi}$ is derived in section 3.5, see equation (33).

3.4. Material frame, angular velocity

To complete the description of the motion, we need to keep track of twist, defined as the rotation of the cross sections about the tangent. Indeed twist gives rise to viscous shear stress in the plane of a cross-section, which affects the dynamics of the thread. With the aim to measure twist, we introduce a triad, denoted $(\underline{d}_1(S, t), \underline{d}_2(S, t), \underline{d}_3(S, t))$, which is rigidly attached to the cross-sections. This triad follows the motion of the surrounding fluid particles and is called the material frame.

The flow inside the thread is shearless in the limit of very thin thread, as explained for instance in the work of Ribe and collaborators [11]. A similar argument holds in the case of elastic rods, see for instance reference [56]. As a result, material cross sections cannot slide with respect to another and remain perpendicular to the local tangent to the centerline. This is known as Kirchhoff kinematical hypothesis, but it can be justified rigorously by asymptotic analysis. Therefore we impose the following conditions: (i) the triad satisfies the orthonormality condition (2), and (ii) it is compatible with the centerline in the sense that

$$\underline{d}_3(S, t) = \underline{t}(S, t). \quad (24)$$

This kinematical condition is at the core of the mechanics of thin threads; it couples the rotations of the material frame, measured using the triad \underline{d}_i in the left-hand side of the equation, with the motion of the centerline whose tangent appears in the right-hand side.

The definition of the Darboux vector in equation (3) yields, after replacing the general parameter σ with time, $\sigma = t$,

$$\frac{\partial \underline{d}_i(S, t)}{\partial t} = \underline{\omega}(S, t) \times \underline{d}_i(S, t) \quad (25)$$

for any value of the index $i = 1, 2, 3$. In the context of time derivation, the Darboux vector $\underline{\Gamma}(t)$ is denoted $\underline{\omega}(S, t)$ and is called the angular velocity vector;

its tangential component is called the axial spin velocity $\Gamma_3 = v(S, t)$,

$$v(S, t) = \underline{\omega}(S, t) \cdot \underline{t}(S, t). \quad (26)$$

By equation (5), v is given by $v = \dot{\underline{d}}_1 \cdot \underline{d}_2$. An explicit expression for the angular velocity is obtained from equation (4):

$$\underline{\omega}(S, t) = \underline{t}(S, t) \times \dot{\underline{t}}(S, t) + v(S, t) \underline{t}(S, t). \quad (27)$$

A second Darboux vector is obtained in the case of spatial derivatives, inserting $\sigma = S$ in equation (3). This vector is associated with infinitesimal changes of the Lagrangian coordinate S , and is called the twist-curvature vector. It is denoted $\underline{\pi}(S, t)$ and satisfies the fundamental relation (3):

$$\frac{\partial \underline{d}_i(S, t)}{\partial S} = \underline{\pi}(S, t) \times \underline{d}_i(S, t), \quad (28)$$

for any value of the index $1 \leq i \leq 3$. Its tangential component is called the (Lagrangian) kinematical twist and noted $\tau(S, t)$ instead of the generic notation Γ_3 :

$$\tau(S, t) = \underline{\pi}(S, t) \cdot \underline{t}(S, t). \quad (29)$$

This scalar $\tau(S, t)$ measures the rate of rotation of the material frame about the tangent: $\tau(s, t) = \underline{d}'_1 \cdot \underline{d}_2$. It is different from the Frénet-Serret notion of torsion for a three-dimensional curve which does not make any reference to the material frame \underline{d}_i . The Frénet-Serret torsion measures the non-planarity of a curve, although the kinematical twist τ can be non-zero even though the centerline is planar, as happens for instance in the case of a straight but twisted configuration.

The normal projection of $\underline{\pi}$ is given by the general expression of the Darboux vector in equation (4), combined with the condition of compatibility (24),

$$\underline{\pi}(S, t) = \underline{K}(S, t) + \tau(S, t) \underline{t}(S, t), \quad (30)$$

where we have introduced the Lagrangian binormal curvature

$$\underline{K}(S, t) = \underline{t}(S, t) \times \frac{\partial \underline{t}(S, t)}{\partial S}. \quad (31)$$

Note $\underline{K}(S, t)$ depends only on the centerline, not on the material frame. Consistently with our Lagrangian approach, both the kinematical twist τ and the binormal curvature \underline{K} refer to a unit increment of the arc length S in the reference configuration, not to the arc length s in the actual configuration. As a result, these quantities differ from the usual twist and curvature used in the Eulerian framework and some care is required when comparing our equations with their Eulerian variants. Equation (30) shows that the tangential component of $\underline{\pi}$ encodes the twist while its normal projection encodes for the curvature, hence the name twist-curvature vector.

The measure of strain relevant to the stretching mode is provided by the extension $\ell(S, t)$ defined earlier in equation (16). This vector $\underline{\pi}(S, t)$ just introduced provides a measure of strain relevant to the two other modes, twisting and bending. For viscous threads, we need to evaluate the *rates of strain*. This is the goal of the next sections: in section 3.5 we derive an identity for the covariant time derivative of $\underline{\pi}(S, t)$, and in section 3.6 we identify this quantity as the rate of strain, which is needed in the constitutive relations.

3.5. Compatibility of rotations

The rotation velocity $\underline{\omega}$ and the twist-curvature vector $\underline{\pi}$ characterize infinitesimal changes of the material frame $\underline{d}_i(S, t)$ corresponding to increments of time t and of arc length S , respectively. A compatibility condition relating the vectors $\underline{\omega}'$ and $\underline{\pi}$ can be derived from the identity of the cross-derivatives in Lagrangian coordinates (t, S) :

$$\frac{\partial}{\partial t} \left(\frac{\partial \underline{d}_i(t, S)}{\partial S} \right) = \frac{\partial}{\partial S} \left(\frac{\partial \underline{d}_i(t, S)}{\partial t} \right).$$

In this expression, we express the innermost derivatives with the help of equations (25) and (28) and write

$$\frac{\partial(\underline{\pi} \times \underline{d}_i)}{\partial t} = \frac{\partial(\underline{\omega} \times \underline{d}_i)}{\partial S}.$$

We use equations (25) and (28) again to expand the derivatives, and find

$$\left(\frac{\partial \underline{\pi}}{\partial t} - \frac{\partial \underline{\omega}}{\partial S} \right) \times \underline{d}_i = -\underline{\pi} \times (\underline{\omega} \times \underline{d}_i) + \underline{\omega} \times (\underline{\pi} \times \underline{d}_i).$$

The right-hand side can be simplified using Jacobi's identity, $\underline{a} \times (\underline{b} \times \underline{c}) + \underline{b} \times (\underline{c} \times \underline{a}) + \underline{c} \times (\underline{a} \times \underline{b}) = \underline{0}$, valid for any set of vectors \underline{a} , \underline{b} , \underline{c} . With $\underline{a} = \underline{\pi}$, $\underline{b} = \underline{\omega}$ and $\underline{c} = \underline{d}_i$, this yields

$$\frac{\partial \underline{\omega}}{\partial S} = \frac{\partial \underline{\pi}}{\partial t} - \underline{\omega} \times \underline{\pi},$$

which is also known as the Maurer-Cartan identity. Here we have simplified by \underline{d}_i , since the relations hold for any value of the index $i = 1, 2, 3$.

In the right-hand side we can identify the covariant derivative defined in section 2.3, here with $\sigma = t$ and $\underline{t} = \underline{d}_3$. It is defined for an arbitrary vector field $\underline{a}(S, t)$ by

$$\frac{\tilde{\partial} \underline{a}(S, t)}{\tilde{\partial} t} = \frac{\partial \underline{a}(S, t)}{\partial t} - \underline{\omega}(S, t) \times \underline{a}(S, t). \quad (32)$$

We can then rewrite the compatibility condition in a compact form,

$$\frac{\partial \underline{\omega}(S, t)}{\partial S} = \frac{\tilde{\partial} \underline{\pi}(S, t)}{\tilde{\partial} t}. \quad (33)$$

Note that the role of $\underline{\omega}$ and $\underline{\pi}$ is symmetric and it is possible to rewrite this equation the other way around,

$$\frac{\partial \underline{\pi}(S, t)}{\partial S} = \frac{\tilde{\partial} \underline{\omega}(S, t)}{\tilde{\partial} t}.$$

However, we shall only make use of equation (33) in the following, as it provides the relevant measure of rate of strain.

3.6. Strain rate vector

The quantities appearing in equation (33) are fundamental for the dynamics of viscous rods, and are related to the strain rates of the different modes of deformation. The left-hand side is denoted \underline{e} :

$$\underline{e} = \frac{\partial \underline{\omega}(S, t)}{\partial S}. \quad (34)$$

The vector \underline{e} , called the *strain rate vector*, provides the measure of the rates of deformation relevant to the twist and curvature modes. As such it appears in the right-hand sides of the constitutive laws obtained by dimensional reduction, see equations (63b). In particular, when the thread undergoes a rigid-body motion, $\underline{\omega}$ is independent of S , the strain rate vector \underline{e} vanishes and so does the viscous stress, as expected.

Let us introduce the projections of $\underline{e}(S, t)$ in the tangential and normal directions, denoted e_t and \underline{e}_b respectively:

$$\underline{e}(S, t) = e_t(S, t) \underline{t}(S, t) + \underline{e}_b(S, t), \quad \underline{e}_b(S, t) \cdot \underline{t}(S, t) = 0. \quad (35)$$

The subscripts are motivated by the fact that the projections are associated with the twisting and bending deformations, respectively, as we show below. The projections are defined by the following explicit formulas,

$$e_t(S, t) = \underline{e}(S, t) \cdot \underline{t}(S, t) \quad (36a)$$

$$\underline{e}_b(S, t) = \underline{P}_\perp(\underline{t}(S, t), \underline{e}(S, t)) \quad (36b)$$

The covariant derivative in the right-hand side of the compatibility condition (33) commutes with the projection by equation (11). As a result, the decomposition of the twist-curvature vector $\underline{\pi}$ in equation (30) implies

$$e_t(S, t) = \frac{\partial \tau(S, t)}{\partial t} \quad (37a)$$

$$\underline{e}_b(S, t) = \frac{\tilde{\partial} \underline{K}(S, t)}{\tilde{\partial} t}. \quad (37b)$$

Here e_t and \underline{e}_b appear to be given by the time-derivative of the strain measures — the kinematical twist τ and the curvature binormal \underline{K} . These derivatives are evaluated in a frame following the material (notice the presence of the covariant derivative in the second equation, and recall that the time derivative in the first

equation is actually a convective derivative as we use Lagrangian variables). Equations (37) confirms that e_t and e_b measure the rates of change of the twist strain τ and of the bending strain \underline{K} , respectively. For the sake of completeness, we recall the definition of the rate of strain associated with the stretching mode of deformation, given earlier in equation (20):

$$d(S, t) = \frac{\partial \ell(S, t)}{\partial t}. \quad (37c)$$

The decomposition of \underline{e} in equation (35), and the interpretations of its projections in equations (37) raise some difficulties in the discrete setting. Indeed, the definition of \underline{e} as the gradient of rotation, given in equation (34), cannot be extended to the discrete case, as we shall see. However it is possible to propose discrete equivalents to its tangent and normal projections e_t and e_b separately.

3.7. A geometrical identity for the twist's rate of strain

We derive in this section a geometric identity which is central to the mechanics of thin elastic rods and viscous threads. It explains the coupling between the motion of the centerline $\underline{x}(S, t)$ and the twist $\tau(S, t)$. In a previous work [35] focusing on the case of elastic rods, this equation was used to obtain a natural discretization of the twist. A similar discretization strategy is followed here.

We start by projecting the compatibility condition (33) along the tangent direction, using the product rule:

$$e_t = \frac{\partial \tau(S, t)}{\partial t} = \underline{t} \cdot \frac{\partial \underline{\omega}}{\partial S} = \frac{\partial(\underline{t} \cdot \underline{\omega})}{\partial S} - \frac{\partial \underline{t}}{\partial S} \cdot \underline{\omega}.$$

By equation (27), we can identify the quantity $(\underline{t} \cdot \underline{\omega})$ appearing in the right-hand side as the angular twist velocity v . In the second term, the time derivative of the tangent is given by combining equations (28) and (24) as

$$e_t = \frac{\partial v(S, t)}{\partial S} - (\underline{\pi} \times \underline{t}) \cdot \underline{\omega}.$$

In the right-hand side, we can replace $\underline{\pi}$ by its transverse projection \underline{K} inside the cross product $\underline{\pi} \times \underline{t}$. We then permute the mixed product and use $\underline{\omega} \times \underline{t} = \dot{\underline{t}}$ by equation (25). Then we find

$$e_t = \frac{\partial v(S, t)}{\partial S} + \underline{K}(S, t) \cdot \frac{\partial \underline{t}(S, t)}{\partial t}. \quad (38)$$

We shall now comment a little on this equation which is important both at a practical and at a fundamental level.

On a practical side, equation (38) makes it possible to use the centerline position $\underline{x}(S, t)$ and the spin velocity $v(S, t)$ as the primary variables for parameterizing the thread. When combined the definitions $\underline{K} = \underline{t} \times \underline{t}'$ and $\underline{t} = \underline{x}'$, equation (38) provides the value of the strain rate for the twisting mode, $e_t = \dot{\tau}$, a quantity that is required in the constitutive law (63b). This centerline/spin parameterization has important benefits, as we shall argue later on.

More fundamentally, equation (38) explains the coupling between the centerline motion and the twisting motion of the material frame: the twisting moment is proportional to the rate of strain e_t , which not only depends on the rotational degree of freedom v (through the first term in the right-hand side) but also on the centerline motion (through the second term). The geometry underlying equation (38) has been discussed by several authors but has never been used as a starting point for setting up simulations of viscous threads. This equation can be seen as an incremental version of the Călugăreanu-White-Füller (CWF) theorem [57, 58, 59, 60, 61] which defines the notion of writhing for a closed curve — for a short review on this theorem, see references [62, 53]. The CWF theorem has become very well known in the context of supercoiled DNA [63, 64, 65, 66] or polymers [67], and has been used in other contexts such as the dynamics of elastic filaments in a viscous fluid [54, 68] or the mechanics of proteins [69]. The binormal curvature $\underline{K}(S, t)$ in the right-hand side of equation (38) above is directly responsible for the geometrically non-linear term $\underline{T} \times \underline{n}$ of the equations of motion, see equation (71). There is no obvious way to discretize this term of the equations of motion, but a natural discretization will become apparent when this term is connected to the geometric context of equation (38), a variant of which will appear in the discrete setting, see equation (100) below.

3.8. Centerline/spin representation

The initial parameterization of the thread introduced in sections 3.2 and 3.4 is based on the centerline position $\underline{x}(S, t)$ and the orthonormal frame $(\underline{d}_i(S, t))$ with $1 \leq i \leq 3$. This parameterization is subjected to the kinematical constraint of compatibility expressed by equation (24). From a numerical viewpoint it is desirable to eliminate this constraint, and use a reduced set of variables instead. To this end we introduce the centerline/spin representation (\underline{x}, v) : the centerline is described using $\underline{x}(S, t)$ as earlier but the material frame is described in an incremental way using the spin velocity $v(S, t)$ introduced in equation (26). By ‘incremental’, we mean that we do not keep track of the absolute direction of the transverse material vectors \underline{d}_1 and \underline{d}_2 but only of the spin velocity $v = \underline{d}_1 \cdot \dot{\underline{d}}_2$. Indeed, in the case of isotropic cross-sections which we consider here, the absolute direction of the material frame can be eliminated from the equations of motion. Our centerline/*spin* representation is inspired from the centerline/*angle* representation introduced by Langer and Singer in the context of elastic rods [53]; while they define the orientation of the cross-section incrementally with respect to arc length S using a twist angle θ , we define it incrementally with respect to time t using a spinning velocity v . The benefit of our representation is that it makes the matrix governing the dynamics of the thread sparse, as explained later. The initial $(\underline{x}, \underline{d}_i)$ representation uses 3 degrees of freedom, such as the Euler angles, for the orientation of the material frame, which are subjected to 2 scalar constraints for the compatibility. By comparison, the centerline/spin representation uses a single degree of freedom $v(S, t)$ for the description of the twisting degree of freedom, which is free of kinematical constraint. This has the important benefit of decreasing the number of degrees of freedom and removing constraints.

In this section and in the next ones, we expose the principle of the time-stepping algorithm in the centerline/spin representation. This algorithm is used at a particular time t to derive positions and velocities at the next time step. In the absence of any ambiguity, we shall often omit the time argument t from now on. The equations of motion being second-order in time, we assume that the actual position, as well as the linear and angular velocities as prescribed,

$$\underline{x}(S) = \underline{x}(S, t), \quad \underline{u}(S) = \dot{\underline{x}}(S, t), \quad \underline{v}(S) = v(S, t). \quad (39)$$

We show how the linear and angular accelerations $\underline{\gamma}(S) = \ddot{\underline{x}}(S)$ and $\dot{v}(S)$ can be computed. This requires reconstructing a number of intermediate quantities.

To begin with, we can readily compute the axial strain $\ell(S)$, the unit tangent \underline{t} and the binormal curvature \underline{K} defined respectively by equations (15), (16), and (31) in terms of the centerline, without even using the velocities:

$$\ell(S) = |\underline{x}'(S)| \quad (40a)$$

$$\underline{t}(S) = \frac{\underline{x}'(S)}{\ell(S)} \quad (40b)$$

$$\underline{K}(S) = \underline{t}(S) \times \underline{t}'(S). \quad (40c)$$

3.9. Reconstruction of strain rates from velocities

We now proceed to the reconstruction of the strain rates d , e_t and e_b defined in equations (37). We introduce a reconstruction scheme valid for arbitrary velocities, denoted $\hat{\underline{u}}$ and \hat{v} , that are not necessarily equal to the velocities \underline{u} and v of the actual motion. These velocities $\hat{\underline{u}}$ and \hat{v} will be called virtual. Working out the dependence of the strain rates on arbitrary (virtual) velocities will enable us to put the constitutive laws in a variational framework, using dissipation potentials. This approach will allow for a natural discretization of the constitutive laws.

We start by reconstructing the time derivative of the tangent, $\dot{\underline{t}}$. By equation (21) this involves the operator $\underline{\mathcal{V}}$

$$\underline{\mathcal{V}}(\underline{x}; \hat{\underline{u}}; S) = \frac{1}{\ell(S)} \underline{P}_\perp(\underline{t}(S), \hat{\underline{u}}'(S)). \quad (41a)$$

Note that $\underline{\mathcal{V}}$ depends on the *functions* \underline{x} and $\hat{\underline{u}}$, and not just on their values at S . In the right-hand side, $\ell(S)$ and $\underline{t}(S)$ are reconstructed from the centerline $\underline{x}(S)$ passed as the first argument of $\underline{\mathcal{V}}$ using equations (40).

In the particular case of the real motion, when the operator is evaluated with the actual velocity $\hat{\underline{u}}(S) = \underline{u}(S) = \dot{\underline{x}}(S, t)$ defined in equation (39), $\underline{\mathcal{V}}$ yields by construction

$$\underline{\mathcal{V}}(\underline{x}; \underline{u}; S) = \frac{\partial \underline{t}(S, t)}{\partial t}. \quad (41b)$$

Before considering the strain rates, we also need to reconstruct the material rotation $\underline{\omega}$. For this purpose, equation (27) suggests introducing the operator

$$\underline{\mathcal{W}}(\underline{x}; \hat{\underline{u}}, \hat{v}; S) = \hat{v}(S) \underline{t}(S) + \underline{t}(S) \times \underline{\mathcal{V}}(\underline{x}; \hat{\underline{u}}; S). \quad (42a)$$

Here again, the tangent \underline{t} is implicitly a function of the first argument \underline{x} . This operator $\underline{\mathcal{W}}$ yields the material rotation in the case of a real motion $\hat{\underline{u}} = \underline{u}$:

$$\underline{\mathcal{W}}(\underline{x}; \underline{u}, v; S) = \underline{\omega}(S, t). \quad (42b)$$

The strain rates d , \underline{e}_t and \underline{e}_b are reconstructed by means of three operators, noted \mathcal{L}_s , \mathcal{L}^t and $\underline{\mathcal{L}}^b$ respectively. The definition of the operator associated with the stretching mode is motivated by equation (20):

$$\mathcal{L}_s(\underline{x}; \hat{\underline{u}}; S) = \underline{t}(S) \cdot \hat{\underline{u}}'(S). \quad (43)$$

When evaluated with a real motion it yields the strain rate,

$$\mathcal{L}_s(\underline{x}; \underline{u}; S) = d(S, t). \quad (44)$$

The twisting and bending strains are introduced through a decomposition equivalent to the one used in equation (35):

$$\frac{d\underline{\mathcal{W}}(\underline{x}; \hat{\underline{u}}, \hat{v}; S)}{dS} = \mathcal{L}^t(\underline{x}; \hat{\underline{u}}, \hat{v}; S) \underline{t}(S) + \underline{\mathcal{L}}^b(\underline{x}; \hat{\underline{u}}, \hat{v}; S), \quad (45)$$

where the right-hand sides are defined by the following projections:

$$\mathcal{L}^t(\underline{x}; \hat{\underline{u}}, \hat{v}; S) = \underline{t}(S) \cdot \frac{d\underline{\mathcal{W}}(\underline{x}; \hat{\underline{u}}, \hat{v}; S)}{dS} \quad (46a)$$

$$\underline{\mathcal{L}}^b(\underline{x}; \hat{\underline{u}}, \hat{v}; S) = \underline{P}_\perp \left(\underline{t}(S), \frac{d\underline{\mathcal{W}}(\underline{x}; \hat{\underline{u}}, \hat{v}; S)}{dS} \right). \quad (46b)$$

Note that the total derivative of $\underline{\mathcal{W}}$ in equation (45) and (46) produce terms proportional to $\hat{\underline{u}}'(S)$ and $\hat{v}'(S)$ according to the definition of $\underline{\mathcal{W}}$ in equation (42a). As a result, the operators \mathcal{L}^t and $\underline{\mathcal{L}}^b$ also depend on the local values of $\hat{\underline{u}}'$ and \hat{v}' .

For a real motion, $\underline{\mathcal{W}}$ evaluates to $\underline{\omega}$ by equation (42b), and so the left-hand side of equation (45) evaluates to the strain rate vector \underline{e} . Comparison of the decompositions (35) and (46) shows that, by construction, the operators $\underline{\mathcal{L}}^t$ and $\underline{\mathcal{L}}^b$ yield in the case of a real motion

$$\mathcal{L}^t(\underline{x}; \underline{u}, v; S) = e_t(S, t) \quad (47a)$$

$$\underline{\mathcal{L}}^b(\underline{x}; \underline{u}, v; S) = \underline{e}_b(S, t). \quad (47b)$$

A more explicit form of the operator \mathcal{L}^t defined in equation (46a) can be found by inserting the definition of $\underline{\mathcal{W}}$ into equation (42a). After some algebra, we find

$$\mathcal{L}^t(\underline{x}; \hat{\underline{u}}, \hat{v}; S) = \hat{v}'(S) + \underline{K}(S) \cdot \underline{\mathcal{V}}(\underline{x}; \hat{\underline{u}}; S), \quad (48a)$$

where \underline{K} is the curvature binormal computed from the centerline configuration \underline{x} using equation (40c). This is an extension of equation (38) to virtual velocities.

All the operators $\underline{\mathcal{V}}$, $\underline{\mathcal{W}}$, \mathcal{L}_s , \mathcal{L}^t , $\underline{\mathcal{L}}^b$ introduced above depend linearly on the virtual velocities $\hat{\underline{u}}$ and \hat{v} . Their discrete equivalents shall allow us to calculate the viscous stress.

3.10. Dissipation potentials

In the Lagrangian framework, internal viscous stress can be described by a Rayleigh potential, see for instance reference [70]. This potential, which plays a role similar to the potential energy for elastic rods, expresses the power dissipated by viscosity during a virtual motion prescribed by the velocities $\hat{\underline{u}}(S)$ and $\hat{v}(S)$. This potential has three contributions, corresponding to the stretching, twisting and bending modes of deformation:

$$\mathcal{D}(\underline{x}; \hat{\underline{u}}, \hat{v}) = \mathcal{D}_s(\underline{x}; \hat{\underline{u}}) + \mathcal{D}_t(\underline{x}; \hat{\underline{u}}, \hat{v}) + \mathcal{D}_b(\underline{x}; \hat{\underline{u}}, \hat{v}). \quad (49)$$

The stretching contribution is proportional to the stretching modulus whose expression is due to Trouton [14]:

$$D(\ell) = 3\mu A(\ell) = \frac{D_0}{\ell^2}, \quad (50)$$

where μ is the fluid's dynamic viscosity. Here $D_0 = 3\mu A_0 = 3\mu(\pi a_0^2)$ is the value of the stretching modulus in reference configuration. The twist modulus C and the bending modulus B read [71, 9]

$$C(\ell) = 2\mu I(\ell) = \frac{C_0}{\ell^2}, \quad B(\ell) = 3\mu I(\ell) = \frac{B_0}{\ell^2}, \quad (51)$$

where $C_0 = 2\mu I_0$ and $B_0 = 3\mu I_0$ are the moduli in reference configurations, and the moment of inertia in reference configuration I_0 is defined in section 3.3.

We propose the following expressions for the stretching, twisting and bending contributions to the Rayleigh potential:

$$\mathcal{D}_s(\underline{x}; \hat{\underline{u}}) = \int_{S_-}^{S^+} \frac{D(\ell(S))}{2\ell(S)} \left(\mathcal{L}_s(\underline{x}; \hat{\underline{u}}; S) \right)^2 dS, \quad (52a)$$

$$\mathcal{D}_t(\underline{x}; \hat{\underline{u}}, \hat{v}) = \int_{S_-}^{S^+} \frac{C(\ell(S))}{2\ell(S)} \left(\mathcal{L}^t(\underline{x}; \hat{\underline{u}}, \hat{v}; S) \right)^2 dS, \quad (52b)$$

$$\mathcal{D}_b(\underline{x}; \hat{\underline{u}}, \hat{v}) = \int_{S_-}^{S^+} \frac{B(\ell(S))}{2\ell(S)} \left(\mathcal{L}^b(\underline{x}; \hat{\underline{u}}, \hat{v}; S) \right)^2 dS. \quad (52c)$$

Here S^- and S^+ denotes the Lagrangian coordinates of the endpoints of the thread. Both S^- and S^+ may depend on time even though this time dependence is implicit for the sake of readability. In all the expressions above, ℓ is a function of the first argument \underline{x} by equation (40). Note that the stretching contribution \mathcal{D}_s does not depend on the rotational degree of freedom \hat{v} but solely on the centerline velocity $\hat{\underline{u}}$. Since \mathcal{L}_s , \mathcal{L}^t and \mathcal{L}^b are linear forms, all contributions \mathcal{D}_s , \mathcal{D}_b and \mathcal{D}_t and the total Rayleigh potential \mathcal{D} are quadratic forms of their velocity arguments $\hat{\underline{u}}$ and \hat{v} . This quadratic dependence reflects the linear character of the viscous constitutive laws.

The expressions introduced in equations (52) for \mathcal{D}_s , \mathcal{D}_t and \mathcal{D}_b will be justified *a posteriori* in section 4.2, by checking that they lead to the correct

constitutive laws. In particular, we will explain the reason for the factor $1/\ell$ in the integrands above.

The Rayleigh potential \mathcal{D} allows the equations of motion for a thin viscous thread to be put in variational form. As noticed by Batty and Bridson [72] in the context of 3D fluids with free boundaries, this variational setting provides a natural discretization of these equations. We follow this general approach, and start by exposing the variational structure of the smooth equations.

3.11. Equations of motion

The main property of the Rayleigh potential is that it gives the viscous force by derivation with respect to the virtual velocity: the resultant of the internal viscous stress on the centerline is given by

$$\underline{P}_v(S, t) = - \left. \frac{\partial \mathcal{D}(\underline{x}; \hat{\underline{u}}, \hat{v})}{\partial \hat{\underline{u}}(S)} \right|_{(\hat{\underline{u}}, \hat{v}) = (\underline{u}, v)} \quad (53a)$$

The notation in the right-hand side must be understood as follows: we first take the functional derivative of the potential with respect to its argument $\hat{\underline{u}}$, and later substitute the velocity arguments with their real values, $\hat{\underline{u}} = \underline{u}$ and $\hat{v} = v$. This quantity \underline{P}_v is the resultant of the internal viscous forces, per unit length dS in reference configuration. It includes the stretching, twisting and bending forces, each contribution being listed in equation (49).

The stress conjugated to the spin velocity v is the twisting moment due to the internal viscous stress in the thread. It is given by a similar formula,

$$Q_v(S, t) = - \left. \frac{\partial \mathcal{D}(\underline{x}; \hat{\underline{u}}, \hat{v})}{\partial \hat{v}(S)} \right|_{(\hat{\underline{u}}, \hat{v}) = (\underline{u}, v)} \quad (53b)$$

In equations (53) the functional derivatives in the right-hand sides are calculated practically by computing the first variation $d\mathcal{D}$ of the Rayleigh potential for small increments of the virtual velocities, denoted $\delta \underline{u}$ and δv , and by identifying the result with

$$- d\mathcal{D}(\underline{x}; \underline{u}, v; \delta \underline{u}, \delta v) = \int_{S_-}^{S_+} (\underline{P}_v \delta \underline{u} + Q_v \delta v) dS. \quad (54)$$

This calculation will be carried out later in section 4.4, when we work out explicit expressions for the net viscous force \underline{P}_v and moment Q_v , and check that they are equivalent with the classical Kirchhoff equations.

In terms of the net viscous force \underline{P}_v and twisting moment Q_v , the balance of linear and angular momentum can be written

$$\rho A_0 \ddot{\underline{x}}(S, t) = \underline{P}_v(S, t) + \underline{P}(S, t) \quad (55a)$$

$$\ell J \dot{v}(S, t) = Q_v(S, t) + Q(S, t). \quad (55b)$$

Here $\underline{P}(S, t)$ is the density of external force and $Q(S, t)$ the density of external twisting moment. These balance laws are for an infinitesimal segment, and

per unit length dS in reference configuration. The factors (ρA_0) and (ℓJ) are its mass and moment of inertia about the tangent, measured per unit reference length dS . Here, J is the moment of inertia per unit length ds in *actual* configuration, given by the usual formula

$$J(\ell) = \iint_{|r|<a} r^2 r \, dr \, d\theta = 2\rho I(\ell). \quad (56)$$

The factor ℓ in the left-hand side of equation (55b) is because an element of reference length dS has a moment of inertia $J \, ds = \ell J \, dS$.

By multiplying both terms of the first equation (55a) by a vector-valued test function $\delta \underline{u}(S)$ and both terms of the second equation (55b) by a scalar-valued test function $\delta v(S)$, we can write the equations of motion (55) in weak form. The motion is such that, for any choice of the functions $\delta \underline{u}(S)$ and $\delta v(S)$ and at any time t ,

$$\int_{S_-}^{S^+} (\rho A_0 \dot{\underline{u}} \cdot \delta \underline{u} + J \dot{v} \delta v) \, dS = -d\mathcal{D}(\underline{x}; \underline{u}, v; \delta \underline{u}, \delta v) + \int_{S_-}^{S^+} (\underline{P} \cdot \delta \underline{u} + Q \delta v) \, dS \quad (57)$$

where $\underline{u}(S, t) = \dot{\underline{x}}(S, t)$ is the actual velocity. In continuum mechanics, the left-hand side is called the virtual work of acceleration, the first term in the right-hand side is the internal virtual work, and the last term is the external virtual work. This weak form of the equations of motion will be useful for going to the discrete case.

3.12. External loading

In equations (55), \underline{P} and Q denote the the force resultant and the twisting moment due to external forces — as opposed to the internal, viscous forces in the thread. Those forces are given per unit length dS in reference configuration. In our validation examples, we consider a thread moving under the action of gravity and surface tension. Contact with the ground is not handled by applying forces but instead by freezing the motion of particles, as explained later in section 7.2: we do not need an explicit expression for these contact forces.

Gravity is represented by a force

$$\underline{P}(S, t) = \underline{P}_g(S, t) = \rho A_0 \underline{g}, \quad Q(S, t) = Q_g(S, t) = 0. \quad (58)$$

We now work out the expression of the effective forces acting on the centerline as a result of surface tension on the lateral boundaries of the thread. Those forces are derived by variation from an energy proportional to the lateral area of these boundaries. In the case of a slender thread which we consider, the capillary energy is written using the following approximation of the lateral area:

$$\mathcal{E}_\gamma(\underline{x}) = \int_{S_-}^{S^+} \gamma 2\pi a(\ell(S)) \ell(S) \, dS, \quad (59)$$

where γ is the surface tension, possibly depending on time and position along centerline, and $2\pi a(\ell) (\ell \, dS)$ is the lateral area of a cylinder of radius a and

length $ds = \ell dS$. We neglect the small conical angle of the lateral surface, which has a negligible influence on the capillary forces for a thin thread.

The effective capillary force acting on the centerline can be obtained by variation, using the definition of $a(\ell)$ in equation (23) and the definition of ℓ in terms of $\underline{x}(S)$ in equation (15). This yields

$$d\mathcal{E}(\underline{x}; \delta \underline{x}) = \left[\underline{n}_\gamma \delta \underline{x} \right]_{S^-}^{S^+} - \int_{S^-}^{S^+} \underline{P}_\gamma(S) \cdot \delta \underline{x} dS, \quad (60a)$$

where the bracket denotes the boundary term coming from the integration by parts, and

$$\underline{P}_\gamma(S, t) = \frac{\partial \underline{n}_\gamma(S, t)}{\partial S} \quad (60b)$$

$$Q_\gamma(S, t) = 0 \quad (60c)$$

$$\underline{n}_\gamma(S, t) = \gamma \pi a(S, t) \underline{t}(S, t). \quad (60d)$$

3.13. Neglecting rotational inertia

For thin elastic rods or viscous threads, a classical approximation, proposed by Kirchhoff himself, is to neglect the rotational inertia, that is to set $J = 0$ in the equation of motion (55b). This approximation can be justified by the fact that the kinetic energy associated with rotational inertia scales like $(\ell J) v^2 \sim \ell \rho a^4 (1/t^*)^2$ for a motion happening on a typical time-scale t^* . By contrast the kinetic energy associated with translation of the centerline scales like $\ell \rho A \underline{u}^2 \sim \ell \rho a^2 (L/t^*)^2$, where L is the typical length-scale of the motion. The energy of the rotational mode is therefore negligible for slender threads, for which $L \gg a$. Rotational inertia is always dominated by translational inertia — except for a straight viscous thread moving in pure twist, a particular case where the kinetic energy in translation is exactly zero and the above argument is inapplicable. Therefore, we set $J = 0$ in the following. The longitudinal balance of angular momentum (55b) becomes a condition for the quasi-static equilibrium of the twisting mode:

$$0 = Q_v(S, t) + Q(S, t). \quad (61)$$

This equation expresses the fact that the typical time associated with the damping of twist waves, which is much shorter than that associated with the damping of bending waves by the above scaling argument, is considered to be shorter than the time step of the simulation.

4. Equivalence with Kirchhoff equations for a thin viscous thread

This section aims at demonstrating the equivalence of the Lagrangian description of threads based on the centerline/spin representation (\underline{x}, v) exposed in the previous section, and the classical Kirchhoff equations for thin viscous

threads. The goal is to bridge the gap with classical formulations, and to identify important stress variables that underlie the dynamic equations derived in the previous section. No new ingredient required in the numerical model will be introduced, and the reader interested only in the implementation can skip ahead to the derivation of the discrete model in section 5.

4.1. Constitutive laws underlying the dissipation potential

To establish the connection between our formalism and the Kirchhoff equations, we shall start by calculating the force \underline{P}_v and twisting moment Q_v arising from viscous stress. By equation (54), this requires working out the first variation of the dissipation potential with respect to the velocities $\hat{\underline{u}}$ and \hat{v} , near the real motion $\hat{\underline{u}} = \underline{u}$ and $\hat{v} = v$. Combining equations (49) and (52), we can write this first variation as

$$-d\mathcal{D}(\underline{x}; \underline{u}, v; \delta \underline{u}, \delta v) = - \int_{S_-}^{S_+} \left(\frac{D \mathcal{L}_s}{\ell} d\mathcal{L}_s(\delta \underline{u}) + \frac{C \mathcal{L}^t}{\ell} d\mathcal{L}^t(\delta \underline{u}, \delta v) + \frac{B \underline{\mathcal{L}}^b}{\ell} \cdot d\underline{\mathcal{L}}^b(\delta \underline{u}, \delta v) \right) dS,$$

where we have temporarily omitted the arguments \underline{x} , \underline{u} , v and S in the integrand for better readability. Since the latter are the real velocities, we can make use of equations (44) and (47), and write

$$-d\mathcal{D}(\underline{x}; \underline{u}, v; \delta \underline{u}, \delta v) = - \int_{S_-}^{S_+} \left(\frac{D d}{\ell} d\mathcal{L}_s(\delta \underline{u}) + \frac{C e_t}{\ell} d\mathcal{L}^t(\delta \underline{u}, \delta v) + \frac{B \underline{e}_b}{\ell} \cdot d\underline{\mathcal{L}}^b(\delta \underline{u}, \delta v) \right) dS, \quad (62)$$

where the omitted arguments \underline{x} , \underline{u} and v again refer to the real motion.

Let us denote n_s the first coefficient appearing in the integrand, and assemble the two other coefficients into a vector denoted \underline{m} :

$$n_s(S, t) = \frac{1}{\ell} (D d) \quad (63a)$$

$$\underline{m}(S, t) = \frac{1}{\ell} (C e_t \underline{t} + B \underline{e}_b). \quad (63b)$$

Note that these coefficients do not depend on the virtual motion but only on the actual one. The quantities introduced in equation (63) will be identified as the viscous stress in the thread. More accurately, n_s is the scalar tension resisting stretching and \underline{m} the internal moment arising from twisting and bending.

The *vector* tension will also be useful later on,

$$\underline{n}_s(S, t) = n_s(S, t) \underline{t}(S, t). \quad (64)$$

It can be interpreted as the internal force that arises in response to stretching deformations.

4.2. Equivalence with Eulerian constitutive laws

The constitutive laws can be rewritten in Eulerian form, which is how they are classically presented in the literature. From equations (63), we have

$$n_s(S, t) = D d^E \quad (65a)$$

$$\underline{m}(S, t) = [C(\underline{t} \otimes \underline{t}) + B(\underline{1} - \underline{t} \otimes \underline{t})] \cdot \underline{e}^E, \quad (65b)$$

where we have introduced the Eulerian strain rate,

$$d^E = \frac{d}{\ell}, \quad \underline{e}^E = \frac{1}{\ell} \underline{e} = \frac{1}{\ell} \frac{\partial \underline{\omega}}{\partial S} = \frac{\partial \underline{\omega}}{\partial s}. \quad (65c)$$

In the square brackets of equation (65b), we have introduced the tensor of viscous moduli. The operators in parentheses inside these square brackets are the tangential and perpendicular projection operators.

In Appendix A, we show that the constitutive laws used in the classical work of Ribe [9], and derived by him from the Stokes equations in 3D, are equivalent to equations (65) above.

We note that, according to the Rayleigh-Taylor analogy, the case of an elastic rod is described by very similar equations, namely by replacing the strain rate \underline{e}^E in the constitutive law (65b) by the Eulerian twist-curvature vector $\underline{\pi}^E$, and the constitutive law (65a) for the internal tension by the condition of inextensibility, $\ell = 1$.

4.3. Canonical form of the internal virtual work

The viscous introduced stress introduced in equations (63) allows equation (62) to be written as

$$-d\mathcal{D}(\underline{x}; \underline{u}, v; \delta \underline{u}, \delta v) = - \int_{S_-}^{S_+} \left(n_s d\mathcal{L}_s(\delta \underline{u}) + \underline{m} \cdot d\mathcal{M}(\delta \underline{u}, \delta v) \right) dS, \quad (66a)$$

where

$$d\mathcal{M}(\underline{x}; \delta \underline{u}, \delta v; S) = \underline{t}(S) d\mathcal{L}^t(\underline{x}; \delta \underline{u}, \delta v; S) + d\mathcal{L}^b(\underline{x}; \delta \underline{u}, \delta v; S). \quad (66b)$$

In this definition of the operator $d\mathcal{M}$, we recognize the first variation of the right-hand side of equation (45) — this can be shown by noting that its right-hand side is linear with respect to the virtual motion $\delta \underline{u}$ and δv . Inserting into the above equation, we find a compact expression for the first variation of the dissipation potential:

$$-d\mathcal{D}(\delta \underline{u}, \delta v) = - \int_{S_-}^{S_+} \left(\underline{n}_s(S) \cdot \frac{d[\delta \underline{u}]}{dS} + \underline{m}(S) \cdot \frac{d[d\mathcal{W}(\delta \underline{u}, \delta v)]}{dS} \right) dS. \quad (67)$$

Here, the first term in the integrand has been rewritten using $n_s d\mathcal{L}_s = n_s(\underline{t} \cdot \delta \underline{u}'(S)) = \underline{n}_s \cdot \delta \underline{u}'(S)$ by equations (43) and (64).

For any real motion, the quantity $\underline{\mathcal{W}}$ evaluates to the angular velocity $\underline{\omega}$ of a cross-section by equation (42a). Therefore $d\underline{\mathcal{W}}$ can be interpreted as the virtual rotation associated with the virtual motion $\delta\underline{u}$ and δv . In view of this, equation (67) is similar to the classical expression for the internal virtual work in a 3D continuum, $-\iiint \underline{\sigma} : \underline{\nabla}(\delta\underline{x}) d^3x$. In the context of thin viscous threads, the 3D stress $\underline{\sigma}$ is replaced by the stretching force \underline{n}_s in the first term and by the bending and twisting moment \underline{m} in the second term, the gradient is replaced by the spatial derivative d/dS , and the virtual displacement $(\delta\underline{x})$ is replaced by the virtual velocity $\delta\underline{u}$ and virtual spin velocity δv .

4.4. Identification of the net viscous force and twisting moment

We shall now derive explicit expressions for the effective force and moment acting on the centerline as a result of the internal viscous stress. Inserting the definition of \mathcal{V} in equation (41a) into the definition of \mathcal{W} in equation (42a) and computing the first variation, we have

$$d\mathcal{W}(\delta\underline{u}, \delta v) = \underline{t} \delta v + \frac{\underline{t} \times \delta\underline{u}'(S)}{\ell}.$$

Inserting into the expression (67) for the virtual internal work, the first variation of the dissipation potential reads

$$-d\mathcal{D}(\delta\underline{u}, \delta v) = -\int_{S_-}^{S_+} \left(\underline{n}_s \cdot \frac{d\delta\underline{u}}{dS} + \underline{m} \cdot \frac{d(\underline{t} \delta v + \frac{1}{\ell} \underline{t} \times \delta\underline{u}'(S))}{dS} \right) dS.$$

We can integrate by parts to cast the right-hand side into a form similar to equation (54):

$$-d\mathcal{D}(\delta\underline{u}, \delta v) = \text{BT} + \int_{S_-}^{S_+} \left(\underline{t} \cdot \frac{\partial \underline{m}}{\partial S} \delta v + \frac{\partial(\underline{n}_s + \frac{1}{\ell} \underline{t} \times \underline{m}'(S))}{\partial S} \cdot \delta\underline{u} \right) dS \quad (68)$$

where BT stands for boundary terms. Those boundary terms are omitted in the smooth case, and will be readily obtained from our variational formulation in the discrete case.

Identifying equations (54) and (68), we find an explicit expression for the net force \underline{P}_v acting on the centerline and for the net twisting moment Q_v :

$$\underline{P}_v(S, t) = \frac{\partial \underline{n}(S, t)}{\partial S} \quad (69a)$$

$$Q_v(S, t) = \underline{t}(S, t) \cdot \frac{\partial \underline{m}(S, t)}{\partial S} \quad (69b)$$

where

$$\underline{n}(S, t) = \underline{n}_s + \frac{1}{\ell(S, t)} \underline{t}(S, t) \times \frac{\partial \underline{m}(S, t)}{\partial S}. \quad (69c)$$

This net force results from the combination of viscous stretching, twisting and bending stresses inside the thread, and has been computed using the Rayleigh dissipation potentials. In these expressions we have omitted pointwise forces and moments at the endpoints $S = S^\pm$ coming from the boundary terms. They will be restored in the discrete model.

4.5. Equivalence with Kirchhoff equations

We proceed to show that the expressions (69) for the net force \underline{P}_v and twisting moment Q_v acting on the centerline are equivalent to the equation of motion for a thin thread due to Kirchhoff.

The Kirchhoff equations are usually written in Eulerian variables as

$$\frac{\partial \underline{n}}{\partial s} + \underline{P}^E = \rho A \ddot{\underline{x}} \quad (70a)$$

$$\frac{\partial \underline{m}}{\partial s} + \underline{t} \times \underline{n} + Q^E \underline{t} = J \dot{\underline{v}} \underline{t} \quad (70b)$$

Here, \underline{P}^E and Q^E are density of applied force and twist per unit length ds in actual configuration, respectively.

When these loads are multiplied by $\ell = \frac{\partial s}{\partial S}$, we obtain our Lagrangian densities of load $\underline{P} = \ell \underline{P}^E$, $Q = \ell Q^E$. Multiplying both equations (70a) and (70b) by ℓ , we have

$$\frac{\partial \underline{n}}{\partial S} + \underline{P} = \rho A_0 \ddot{\underline{x}} \quad (71a)$$

$$\frac{\partial \underline{m}}{\partial S} + \underline{T} \times \underline{n} + Q \underline{t} = \ell J \dot{\underline{v}} \underline{t} \quad (71b)$$

where $A_0 = \ell A$ is the area of the cross-section in reference configuration, and $\underline{T} = \ell \underline{t}$ is the deformed (non-unit) material tangent defined in equation (14).

Projecting equation (71b) along the tangent and normal directions successively, we have

$$\underline{t} \cdot \frac{\partial \underline{m}}{\partial S} + Q = \ell J \dot{\underline{v}} \quad (71c)$$

$$\underline{P}_\perp(\underline{t}, \underline{n}) = \frac{1}{\ell} \underline{t} \times \frac{\partial \underline{m}}{\partial S} \quad (71d)$$

The tangential component of the internal force \underline{n} can be interpreted as that resisting stretching of the centerline. It is called the tension and is denoted \underline{n}_s . The full internal force \underline{n} can then be reconstructed by combining this tangential component $\underline{n}_s = n_s \underline{t}$ with its normal component, given by equation (71d):

$$\underline{n} = \underline{n}_s + \frac{1}{\ell} \underline{t} \times \frac{\partial \underline{m}}{\partial S} \quad (72a)$$

Comparison of equations (71a) and (55a) reveals that the viscous stress, described by the quantities \underline{n} and \underline{m} , produces an net force

$$\underline{P}_v = \frac{\partial \underline{n}}{\partial S} \quad (72b)$$

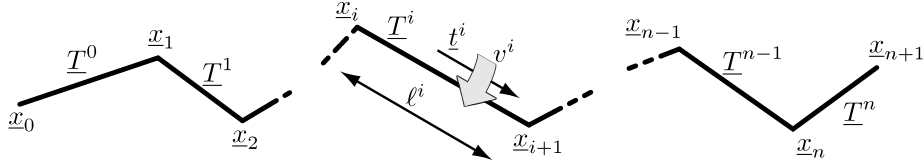


Figure 3: Discrete setting: centerline is a polygonal curve. Note that we use subscripts for vertex-based quantities, such as vertex positions, and superscripts for segment-based quantities, such as segment length ℓ^i .

on the centerline. Similarly, comparison of equations (55b) and (71c) reveals that the net twisting moment due to viscous forces reads

$$Q_v = \underline{t} \cdot \frac{\partial \underline{m}}{\partial S} \quad (72c)$$

The expressions (72b) and (72c) for \underline{P}_v and Q_v derived from the Kirchhoff equations (70) are identical to those derived earlier in equations (69) from our dissipation potentials, based on the centerline/twist representation. We have therefore established the equivalence of our formalism with the classical, Eulerian equations for thin viscous threads. The benefit of our formalism is that it can be discretized in a natural way, and leads to an efficient implementation.

5. Space discretization: the discrete viscous thread model

In this section, the spatial discretization is carried out, by closely following the smooth formalism of the previous sections. Our derivation of the discrete model makes use of three key ideas that have been exposed in the smooth setting. First, we extend the centerline/spin representation to the discrete case; its benefit is to eliminate two out of three rotational degrees of freedom using the condition of compatibility of the tangent. Second, we introduce a discrete twist using the geometrical notion of parallel transport. Third, we derive equations of motion in the discrete setting by variational principles, starting from discrete dissipation potentials.

We start our analysis of spatial discretization by defining discrete quantities such as centerline position, linear and angular velocities, rate of strain, etc. Time discretization will not be discussed until section 6.

5.1. Kinematics of centerline

The centerline is discretized using $(n + 2)$ vertices. Their positions in space are noted $\underline{x}_0(t)$, $\underline{x}_1(t)$, \dots , $\underline{x}_{n+1}(t)$, see figure 3. Our numerical model involves setting up a force, assigning a mass, and integrating the fundamental law of dynamics at each vertex $\underline{x}_i(t)$. The thin thread behavior is produced by means of a discrete viscous force, which by design converges to the force $\underline{P}_v(S, t)$ defined in equations (53a) and (69) in the smooth limit, $n \rightarrow \infty$.

The segment joining vertices \underline{x}_i and \underline{x}_{i+1} is noted

$$\underline{T}^i(t) = \underline{x}_{i+1}(t) - \underline{x}_i(t), \quad (73)$$

as shown in figure 3. Following classical conventions, we use subscripts for indices $0 \leq i \leq n+1$ associated with vertices, and superscripts for indices $0 \leq i \leq n$ associated with segments. Since the vertex index i plays the role of the Lagrangian coordinate S , the segment vector $\underline{T}^i(t)$ defined above is the discrete equivalent of the material, non-unit tangent $\underline{T}(S, t)$ defined in equation (14). More accurately it is, like many other discrete quantities introduced next, an *integrated* quantity: the discrete tangent is essentially the smooth tangent multiplied by the discretization length.

The discrete segment length $\ell^i(t)$ and unit tangent $\underline{t}^i(t)$ are defined by formulas similar to equations (15–16)

$$\ell^i(t) = |\underline{T}^i(t)|, \quad (74)$$

$$\underline{t}^i(t) = \frac{\underline{T}^i(t)}{\ell^i(t)}. \quad (75)$$

We define the vertex velocities by

$$\underline{u}_i(t) = \frac{d\underline{x}_i(t)}{dt}. \quad (76)$$

In terms of the velocities $\underline{u}_j(t)$, we define the integrated axial strain rate for segment \underline{T}^i :

$$d^i(t) = \frac{d\ell^i(t)}{dt} = \underline{t}^i(t) \cdot (\underline{u}_{i+1}(t) - \underline{u}_i(t)), \quad (77)$$

in analogy with equations (17) and (20). This is again an integrated form of the smooth strain rate $d(S, t)$.

The time derivative of the unit tangent is given in terms of the vertex velocities by a geometrical formula analogous to equation (21),

$$\dot{\underline{t}}_i(t) = \frac{1}{\ell^i(t)} \underline{P}_\perp (\underline{t}^i(t), \underline{u}_{i+1}(t) - \underline{u}_i(t)). \quad (78)$$

To define the bending strain, we shall later need vertex-based tangents. There are several possible definitions that are equivalent in the smooth limit, and we opt for one that preserves the unit character of the tangent, namely

$$\tilde{\underline{t}}_i(\underline{x}_{i-1}, \underline{x}_i, \underline{x}_{i+1}) = \frac{\underline{t}^{i-1} + \underline{t}^i}{|\underline{t}^{i-1} + \underline{t}^i|}. \quad (79)$$

The tilde notation is used here and in several other places when we introduce vertex-based versions of quantities that are primarily defined at segments, and *vice-versa*.

Similarly, there are several possible definitions for the discrete binormal curvature vector. One particular definition is:

$$\underline{K}_i(t) = \frac{\underline{t}^{i-1} \times \underline{t}^i}{\frac{1}{2} (1 + \underline{t}^{i-1} \cdot \underline{t}^i)}. \quad (80)$$

The motivation for choosing this particular definition comes from the forthcoming equation (100): this particular expression \underline{K}_i will emerge from the calculation of the discrete twist. The vector \underline{K}_i is an integrated measure of the smooth binormal curvature vector $\underline{K}(S, t)$ defined in equation (31). Indeed the denominator in equation (80) converges to 1 in the smooth limit where $\underline{t}^{i-1} \sim \underline{t}^i \sim \underline{t}(S, t)$, while the numerator is equivalent to $\underline{t}^{i-1} \times \underline{t}^i \sim \underline{t}^{i-1} \times (\underline{t}^i - \underline{t}^{i-1}) \sim \underline{K}(S, t) \tilde{\ell}_i$ where $\tilde{\ell}_i$ is the length of the Voronoi cell around vertex \underline{x}_i , defined below in equation (82).

5.2. Incompressibility: radius and related quantities

Each segment \underline{T}^i carries a volume of fluid V^i and a mass of fluid m^i . Those quantities are initialized based on the prescribed initial segment length, radius and mass density of the fluid. They are conserved during the simulation, except in the case of an adaptive mesh, discussed in section 6.5, which requires segment subdivision. As in the smooth case we use incompressibility to reconstruct the local radius $a^i(t)$ and cross-sectional area $A^i(t)$, assuming that each segment has a cylindrical geometry:

$$A^i(t) = \frac{V^i}{\ell^i(t)}, \quad a^i(t) = \left(\frac{A^i(t)}{\pi} \right)^{1/2}. \quad (81)$$

We shall need later the length $\tilde{\ell}_i$ of the Voronoi region near a given vertex. For an interior vertex \underline{x}_i with $1 \leq i \leq n$, it is defined as the curvilinear distance between the midpoints of the adjacent segments, measured along the polygonal line traced out by the vertices:

$$\tilde{\ell}_i(t) = \frac{\ell^{i-1}(t) + \ell^i(t)}{2} \quad \text{for } 1 \leq i \leq n. \quad (82)$$

This is a vertex-based discretization length, as opposed to the original segment-based discretization length ℓ^j . This length is not required for the end vertices, $i = 0$ and $n + 1$.

5.3. Material frame, angular velocity

The unit tangent \underline{t}^i is defined at segments. We define the orthonormal triads $(\underline{d}_1^i, \underline{d}_2^i, \underline{d}_3^i)$ at the segments too. This allows the condition of compatibility in equation (24) to be easily extended to the discrete case:

$$\underline{d}_3^i(t) = \underline{t}^i(t). \quad (83)$$

Repeating the argument of section 3.4, one can show that the angular rotation $\underline{\omega}^i$ of the material frame can be decomposed as

$$\underline{\omega}^i(t) = v^i(t) \underline{t}^i(t) + \underline{t}^i(t) \times \dot{\underline{t}}^i(t). \quad (84)$$

In the first term of the right-hand side, the quantity $v^i(t)$ is the spin velocity, *i. e.* the angular velocity of the material frame about the tangent, as shown in figure 3. The second term warrants that the time evolution of the centerline, $\dot{\underline{t}}^i = \underline{\omega}^i \times \underline{t}^i$ remains consistent with the condition of compatibility in equation (83).

5.4. Revisiting the case of zero twist: parallel transport

The main difficulty in setting up a discrete model for thin viscous thread resides in the definition of twist. In the smooth case, twist is defined by projecting the infinitesimal rotation vector $\underline{\pi}$ along the tangent. This operation is no longer possible in the discrete case, as rotations are finite and are represented by a matrix. To remedy this difficulty, we introduce the geometrical notion of parallel transport. It enables us to revisit the notion of twist, in a way that makes its extension to the discrete setting natural.

For a given configuration of the centerline, parallel transport defines a series of rotations from one segment to the next. Those rotations define a minimalist motion along the centerline, and will be used to define twist-less states of the thread. Parallel transport has also been used in the smooth setting to define the so-called natural or Bishop frame [52, 53].

Consider the unit tangents \underline{t}^{i-1} and \underline{t}^i of the segments adjacent to a vertex \underline{x}_i . We shall assume that these tangents are not opposite to each other,

$$\underline{t}^{i-1} \neq -\underline{t}^i. \quad (85)$$

This assumption is satisfied, except for a subset of configurations whose measure is zero.

For a reason that will be clear in the next section, we define a rotation \underline{Q} to be *compatible* at vertex \underline{x}_i if it maps \underline{t}^{i-1} to \underline{t}^i :

$$\underline{Q} \cdot \underline{t}^{i-1} = \underline{t}^i. \quad (86)$$

Next, we define parallel transport across vertex \underline{x}_i as *the minimal rotation that is compatible*; here, the word ‘minimal’ refers to the rotation having the smallest possible angle of rotation about its own axis¹. This defines a unique rotation under the assumption of equation (85), as we show now.

Parallel transport, defined above in geometrical terms, has an explicit representation: it is the rotation \underline{T}_i whose axis is along the binormal \underline{K}_i and whose angle is the turning angle φ_i across vertex \underline{x}_i . The turning angle is defined by

$$\varphi_i = \cos^{-1}(\underline{t}^{i-1} \cdot \underline{t}^i) \quad \text{with } 0 \leq \varphi_i < \pi. \quad (87)$$

¹In geometrical terms, this minimal rotation minimizes the distance to the identity over the Lie group of direct rotations in Euclidean 3D space.

Note that $\varphi_i \neq \pi$ by equation (85). The rotation \underline{T}_i just defined satisfies

$$\underline{T}_i^T \cdot \underline{T}_i = \underline{1} \quad (88a)$$

$$\underline{T}_i \cdot \underline{K}_i = \underline{K}_i \quad (88b)$$

$$\underline{T}_i \cdot \underline{t}^{i-1} = \underline{t}^i \quad (88c)$$

These equations express the fact that \underline{T}_i is a rotation, that its axis is aligned with binormal \underline{K}_i , and that it is compatible — compare with equation (86). Compatibility follows from prescribing the rotation angle to be the turning angle φ_i . In the particular case $\varphi_i = 0$, that is when the adjacent segments are aligned, $\underline{t}^{i-1} = \underline{t}^i$, the three equations above no longer define a unique rotation; in this case, parallel transport is defined to be the identity,

$$\underline{T}_i = \underline{1} \quad \text{if } \varphi_i = 0. \quad (88d)$$

Since a compatible rotation maps \underline{t}^{i-1} and \underline{t}^i , its angle of rotation has to be greater or equal to the angle φ_i between them. The angle of rotation of the matrix \underline{T}_i that we have just defined is precisely φ_i . Therefore, to show that the geometric definition parallel transport uniquely defines the matrix \underline{T}_i , it remains to prove that any other compatible rotation has an angle of rotation strictly larger than φ_i . This is what we do now.

First note that any compatible rotation \underline{Q} can be decomposed as

$$\underline{Q} = \underline{T}_i \cdot \underline{R}(\underline{t}^{i-1}, \tau(\underline{Q})) \quad (89)$$

for some angle $\tau(\underline{Q})$. Here $\underline{R}(\underline{t}^{i-1}, \tau)$ denotes the rotation about \underline{t}^{i-1} with angle τ . This decomposition follows from the remark that $\underline{T}_i^{-1} \cdot \underline{Q}$ is a rotation leaving \underline{t}^{i-1} invariant. Denoting \underline{q}_σ the unit vector obtained by rotating \underline{t}^{i-1} about the binormal by an angle σ , one can compute the dot product of \underline{q}_σ with its image $\underline{q}'_\sigma = \underline{Q} \cdot \underline{q}_\sigma$ by the rotation \underline{Q} in equation (89) as

$$\underline{q}_\sigma \cdot \underline{q}'_\sigma = \cos \varphi_i + [\sin(\varphi_i - \sigma) \sin(\sigma)] (1 - \cos \tau(\underline{Q})). \quad (90)$$

This equality can be established in the direct orthonormal basis whose first and last vectors are \underline{t}^{i-1} and $\underline{K}_i/|\underline{K}_i|$, respectively; in this frame, $\underline{q}_\sigma = \{\cos \sigma, \sin \sigma, 0\}$ and $\underline{t}^i = \{\cos \varphi_i, \sin \varphi_i, 0\}$. Details of the calculation are left to the reader.

For any value of φ_i such that $0 \leq \varphi_i < \pi$, there exists at least a value of σ that makes the function inside the square bracket of equation (90) negative and non-zero. If $\cos \tau(\underline{Q}) \neq 1$, this implies

$$\underline{q}_\sigma \cdot \underline{q}'_\sigma < \cos \varphi_i. \quad (91)$$

If the rotation \underline{Q} of equation (89) is different from \underline{T}_i , $\cos \tau(\underline{Q}) \neq 1$. Then equation (91) shows that the angle of rotation of \underline{Q} about its own axis is greater

or equal than $\cos^{-1}(\underline{q}_\sigma \cdot \underline{q}'_\sigma)$, and therefore strictly larger than φ_i . The proof is complete: there is a unique compatible rotation whose angle of rotation is minimal, and this is the rotation $\underline{\underline{T}}_i$ defined in equation (88). It will be called parallel transport.

Parallel transport establishes a natural mapping between cross-sections belonging to neighboring segments, and is similar to the notion of a Levi-Civita connection in differential geometry, see e. g. the book by Wald [73]. This property will now be used to define the discrete twist. More accurately, we shall define twist-less configurations of the rod to be those obtained by parallel-transporting the material frames from one segment to the next, and will *define discrete twist by difference with parallel transport*.

The identification of parallel-transport with twist-less configurations of the rod can be justified by examining compatible rotations in the smooth case. Infinitesimal rotation $\underline{\pi}$ are compatible when they can be associated with material frames satisfying the compatibility condition in equation (24). Such vectors $\underline{\pi}$ are of the form $\underline{\pi} = \underline{K} + \tau \underline{t}$ by equation (30). For a given configuration of the centerline, the binormal curvature \underline{K} is prescribed but τ is a free function. Smooth parallel transport is defined, as in the discrete case, by minimizing the magnitude $|\underline{\pi}|$ of the infinitesimal rotation, keeping the centerline fixed; this minimization yields $\tau(S, t) = 0$. This result confirms that parallel transport is associated with twist-less configurations of the rod in the smooth case. In view of this, it makes sense to use parallel transport to extend the notion of twist to the discrete setting.

5.5. Discrete twist

Since material frames are orthonormal, there exists a unique rotation mapping one material frame to the next. The rotation connecting the two material frames adjacent to the vertex \underline{x}_i is denoted $\underline{\underline{Q}}_i$,

$$\underline{d}_j^i = \underline{\underline{Q}}_i \cdot \underline{d}_j^{i-1} \quad \text{for } j = 1, 2, 3. \quad (92)$$

This finite rotation is the discrete equivalent of the infinitesimal rotation vector $\underline{\pi}(S, t)$ defined in equation (28); in the smooth case, the kinematical twist has been extracted from $\underline{\pi}$ by projection along the local tangent direction. This operation is no longer possible with the finite rotation matrix $\underline{\underline{Q}}_i$.

Parallel transport provides an alternative route for defining twist in the discrete case. To begin with, note that setting $j = 3$ in equation (92) shows that $\underline{\underline{Q}}_i$ is compatible — compare with equation (86), using $\underline{d}_3^j = \underline{t}^j$. Being a compatible rotation, $\underline{\underline{Q}}_i$ can be decomposed using parallel transport, as earlier in equation (89),

$$\underline{\underline{Q}}_i = \underline{T}_i \cdot \underline{\underline{R}}(\underline{t}^{i-1}, \tau_i) = \underline{\underline{R}}(\underline{t}^i, \tau_i) \cdot \underline{T}_i. \quad (93)$$

Here, we use the notation $\tau_i = \tau(\underline{\underline{Q}}_i)$. The alternative decomposition after the second equal sign in equation (93) follows from the following argument: the rotation $[\underline{T}_i \cdot \underline{\underline{R}}(\underline{t}^{i-1}, \tau_i) \cdot \underline{T}_i^T]$ is a rotation of angle τ_i , being conjugated with

$\underline{R}(\underline{t}^{i-1}, \tau_i)$, and in addition leaves \underline{t}^i invariant — it is therefore the rotation about \underline{t}^i with angle τ_i , which is noted $\underline{R}(\underline{t}^i, \tau_i)$. Note that the angle τ_i is uniquely defined modulo 2π .

In equation (93), the angle τ_i defines an axial rotation required to match one material frame to the next, in complement with parallel transport \underline{T}_i . This τ_i is called the discrete angle of twist across vertex \underline{x}_i . It is an integrated version of the kinematical twist $\tau(S, t)$ appearing in the smooth setting.

Let us check that the discrete twist τ_i is consistent with the smooth twist $\tau(S, t)$ in the smooth limit. In equation (93), the rotations \underline{Q}_i , \underline{T}_i and $\underline{R}(\underline{t}^i, \tau_i)$ converge in the smooth limit towards infinitesimal rotations which are represented by the vectors $\underline{\pi}$, \underline{K} and $\tau_i \underline{t}$ respectively; the proof of this is left to the reader. In this limit, equation (93) becomes $\underline{\pi} = \underline{K} + \tau_i \underline{t}$, and we recover the decomposition in equation (30). This confirms that our definition of the discrete twist is consistent in the smooth limit.

5.6. Rate of change of twisting strain

To simulate the dynamics of viscous threads, we need an expression for the rate of strain associated with the twist mode. By analogy with the smooth case, it is defined as the material derivative of the angle of twist,

$$e_i^t = \dot{\tau}_i. \quad (94)$$

Like the quantity τ_i , this is a spatially integrated form of the smooth rate of strain $e_t(S, t)$. The goal of the present section is compute e_i^t in a form that can be used in our centerline/spin representation, i. e. to express e_i^t as a function of the velocities \underline{u}_j and v^j .

To this end, let us start by introducing the polar angles τ_i^- and τ_i^+ of the binormal \underline{K}_i in the frames $(\underline{d}_1^{i-1}, \underline{d}_2^{i-1})$ and $(\underline{d}_1^i, \underline{d}_2^i)$, respectively. These angles are represented in figure 4. They can be computed by taking the arctangent of the coordinates of the vector $\underline{t}^{i-1} \times \underline{t}^i$, which is aligned with \underline{K}_i by definition of the latter. These coordinates are denoted $(\tau_{i1}^-, \tau_{i2}^-)$ in the first frame and $(\tau_{i1}^+, \tau_{i2}^+)$ in the second frame:

$$\tau_i^\pm = \tan^{-1} \left(\frac{\tau_{i2}^\pm}{\tau_{i1}^\pm} \right), \quad (95a)$$

where

$$\tau_{ij}^\pm = (\underline{t}^{i-1} \times \underline{t}^i) \cdot \underline{d}_j^{i+(\pm 1-1)/2}. \quad (95b)$$

In the second equation, j takes on the values 1 or 2, and the superscript in the last factor evaluates to the index $(i-1)$ of the segment in the left-hand side when $\pm = -$, and to the index (i) of the segment in the right-hand side when $\pm = +$.

As shown graphically in figure 4, the rotation \underline{Q}_i can be decomposed into a rotation about \underline{t}^{i-1} with angle τ_i^- that brings \underline{d}_1^{i-1} onto the binormal \underline{K}_i , composed by the parallel transport that maps \underline{t}^{i-1} to \underline{t}^i without affecting the

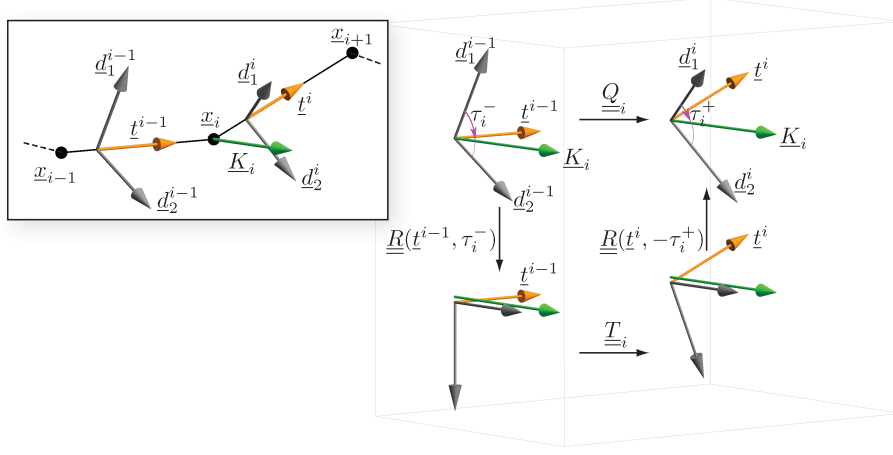


Figure 4: Illustration of equation (96). The rotation mapping one material frame to the next is decomposed using parallel transport and the polar angles τ_i^- and τ_i^+ .

binormal, and composed by a rotation about \underline{t}^i with angle $(-\tau_i^+)$ that brings back the binormal to \underline{d}_1^i without affecting the tangent:

$$\underline{\underline{Q}}_i = \underline{\underline{R}}(\underline{t}^i, -\tau_i^+) \cdot \underline{\underline{T}}_i \cdot \underline{\underline{R}}(\underline{t}^{i-1}, \tau_i^-). \quad (96)$$

As earlier in equation (93), we can use conjugation to group the axial rotations in equation above. Identifying the result with the definition of τ_i in equation (93), we have

$$\tau_i = \tau_i^- - \tau_i^+.$$

Inserting into the definition (94) of the strain rate, we have

$$e_i^t = \dot{\tau}_i^- - \dot{\tau}_i^+. \quad (97)$$

We proceed to compute the time derivatives $\dot{\tau}_i^\pm$ by differentiating equations (95).

The calculation of $\dot{\tau}_{i\alpha}^-$ is done in the frame moving with the first material frame $(\underline{d}_j^{i-1})_{1 \leq j \leq 3}$. There, all vectors in the right-hand side of equation (95b) are still, except \underline{t}^i which has angular velocity $\underline{\omega}^i - \underline{\omega}^{i-1}$. This yields, for $j = 1, 2$,

$$\dot{\tau}_{ij}^- = (\underline{t}^{i-1} \times [(\underline{\omega}^i - \underline{\omega}^{i-1}) \times \underline{t}^i]) \cdot \underline{d}_j^{i-1} = -(\underline{t}^{i-1} \times \underline{d}_j^{i-1}) \cdot [(\underline{\omega}^i - \underline{\omega}^{i-1}) \times \underline{t}^i],$$

after permutation of the mixed product. Inserting this expression into the derivative of the arctangent in equation (95a), we find

$$\dot{\tau}_i^- = \frac{\tau_{i1}^- \dot{\tau}_{i2}^- - \tau_{i2}^- \dot{\tau}_{i1}^-}{(\tau_{i1}^-)^2 + (\tau_{i2}^-)^2} = \frac{(\underline{t}^{i-1} \times \underline{t}^i) \cdot [(\underline{\omega}^i - \underline{\omega}^{i-1}) \times \underline{t}^i]}{|\underline{t}^{i-1} \times \underline{t}^i|^2}. \quad (98a)$$

The time derivative of the second angle τ_i^+ is given by the same formula, with the indices i and $i-1$ swapped:

$$\dot{\tau}_i^+ = \frac{(\underline{t}^{i-1} \times \underline{t}^i) \cdot [(\underline{\omega}^i - \underline{\omega}^{i-1}) \times \underline{t}^{i-1}]}{|\underline{t}^{i-1} \times \underline{t}^i|^2}. \quad (98b)$$

Inserting this expression into equation (97) and permuting the mixed product, we have

$$e_i^t = (\underline{\omega}^i - \underline{\omega}^{i-1}) \cdot \frac{(\underline{t}^i - \underline{t}^{i-1}) \times (\underline{t}^{i-1} \times \underline{t}^i)}{|\underline{t}^{i-1} \times \underline{t}^i|^2}$$

In the right-hand side, the second factor can be simplified using the fact that both \underline{t}^{i-1} and \underline{t}^i are unit vectors. This yields

$$e_i^t = (\underline{\omega}^i - \underline{\omega}^{i-1}) \cdot \frac{\underline{t}^{i-1} + \underline{t}^i}{1 + \underline{t}^{i-1} \cdot \underline{t}^i}. \quad (99)$$

Inserting now the decomposition (84) of the material velocity $\underline{\omega}^j$ and simplifying, we have

$$e_i^t = v^i - v^{i-1} + \underline{K}_i \cdot \frac{\dot{\underline{t}}^{i-1} + \dot{\underline{t}}^i}{2}, \quad (100)$$

after using the definition (80) of the discrete binormal curvature \underline{K}_i .

This formula is fundamental as it yields the rate of strain for the twisting mode in a form that is suitable for our centerline/twist representation. It closely resembles the smooth equation (38). The second term in the right-hand side has a geometrical origin. It captures the change of parallel transport resulting from a change in the centerline, an effect that was dubbed holonomy in our previous work. The holonomy term is responsible for the coupling of centerline motion with the twisting mode, a phenomenon which appears to be geometrical in essence.

The geometrical origin of this coupling has been recognized earlier but has not been used as a starting point for dynamical simulations of threads, to the best of our knowledge. The role of the binormal curvature \underline{K} has been noted in the related context of Füller's theorem [61] for the increment of writhe of a space curve. Expressions similar to those in equations (98) have been derived for the increment of discrete writhe, and have been used for the simulation of the Brownian dynamics of DNA modelled as an elastic rod [74].

5.7. Rate of change of bending strain

In the smooth case, we have defined in equation (34) the strain rate vector $\underline{e}(S, t)$ to be the gradient of rotation. We introduce similarly a discrete strain rate vector \underline{e}^i by

$$\underline{e}^i = \underline{\omega}^i - \underline{\omega}^{i-1}. \quad (101)$$

In equation (35), we have shown that the tangent and perpendicular projections of \underline{e} are the rates of strain relevant to the twisting and bending modes, respectively. In the discrete case, we carry out a similar decomposition, using the vertex-based tangent $\tilde{\underline{t}}_i$,

$$e_i^t = h_t(\varphi_i) \tilde{\underline{t}}_i \cdot \underline{e} \quad \underline{e}_i^b = h_b(\varphi_i) \underline{P}_\perp(\tilde{\underline{t}}_i, \underline{e}_i). \quad (102)$$

In these projections, we have introduced two normalizing functions h_t and h_b of the turning angle φ_i . These functions reflect the fact that the definition of the

vertex-based tangent $\tilde{\underline{t}}_i$ in equation (79) is somewhat arbitrary. For instance, we could use instead a different vertex-based tangent,

$$\tilde{\underline{t}}_i' = \frac{\underline{t}^{i-1} + \underline{t}^i}{1 + \underline{t}^{i-1} \cdot \underline{t}^i} = h(\varphi_i) \tilde{\underline{t}}_i. \quad (103)$$

Here $h(\varphi_i) = |\tilde{\underline{t}}_i'| = 1/\cos(\varphi_i/2)$, as can be shown by using trigonometric relations in the triangle whose sides are \underline{t}^{i-1} and \underline{t}^i . For consistency with the smooth case, we require that the functions h_t and h_b converge to one when their argument vanishes.

Our definition of a discrete twist based on parallel transport imposes a particular choice of the function h_t . Indeed, identifying equations (99) and (103) we find $\underline{e}_i^t = \tilde{\underline{t}}_i' \cdot \underline{e}$ and so $h_t(\varphi_i) = h(\varphi_i) = |\tilde{\underline{t}}_i'| = 1/\cos(\varphi_i/2)$.

By contrast, any choice of the function $h_b(\varphi_i)$ is acceptable as long as $h_b \rightarrow 1$ for $\varphi_i \rightarrow 0$. This leads to infinitely many different discrete thread models, which are all equivalent in the smooth limit. In this paper, we choose $h_b(\varphi_i) = 1$ for simplicity: the strain rate associated with the bending mode then reads

$$\underline{e}_i^b = \underline{P}_\perp(\tilde{\underline{t}}_i, \underline{e}_i). \quad (104)$$

5.8. Reconstruction of strain rates from velocities

As in the smooth case, we keep track of the dependence of all secondary quantities on the velocities, and introduce virtual vertex velocities $\hat{\underline{u}}_i$ and virtual spin velocities v^i at the segments. This shall enable us to compute the discrete viscous forces as the gradient of the dissipation potential with respect to velocities.

The vertex positions are collected into a generalized coordinate $\underline{X}(t)$, a vector of dimension $3(n+2)$:

$$\underline{X}(t) = \{\underline{x}_0(t), \dots, \underline{x}_{n+1}(t)\}. \quad (105)$$

Note that there is no need to keep track of the orientation of the material frame in the generalized coordinate $\underline{X}(t)$, as we consider isotropic cross-sections. The twisting mode will only be included in the generalized velocity $\underline{U}(t)$, defined later, through which it gets coupled with the centerline motion.

Given the centerline configuration $\underline{X}(t)$, we first compute all quantities, such as $\ell^i(\underline{X})$, $\underline{t}^i(\underline{X})$, $\tilde{\underline{t}}_i(\underline{X})$ and $\underline{K}_i(\underline{X})$, which do not depend on velocities. To make the notations lighter, the argument \underline{X} will often not appear explicitly in the following. Next, we extend the operators $\underline{\mathcal{V}}$ and $\underline{\mathcal{W}}$ defined in equations (41) and (42) to the discrete setting. The operator $\underline{\mathcal{V}}^i$ is attached to segment \underline{T}^i and defined by

$$\underline{\mathcal{V}}^i(\underline{X}; \hat{\underline{u}}_i, \hat{\underline{u}}_{i+1}) = \frac{1}{\ell^i} \underline{P}_\perp(\underline{t}^i, \hat{\underline{u}}_{i+1} - \hat{\underline{u}}_i). \quad (106a)$$

This definition comes from equation (78): by design, this operator yields the time derivative of the tangent when applied to a real motion, as in the smooth case.

The discrete operator $\underline{\mathcal{W}}^i$ associated with the segment \underline{T}^i is defined by

$$\underline{\mathcal{W}}^i(\underline{X}; \underline{\hat{u}}_i, \underline{\hat{u}}_{i+1}, \hat{v}^i) = \hat{v}^i \underline{t}^i + \underline{t}^i \times \frac{\underline{\hat{u}}_{i+1} - \underline{\hat{u}}_i}{\ell^i}. \quad (106b)$$

This definition is motivated by equation (84): when evaluated with a real motion, $\underline{\mathcal{W}}^i$ yields the angular velocity vector $\underline{\omega}^i$.

We now propose discrete versions of the three fundamental linear forms defining the viscous dissipation potential, which have been introduced previously in equations (43) and (46).

The discrete axial strain rate d^i on segment \underline{T}^i is given by equation (77). In view of this, we introduce the linear form

$$\mathcal{L}_s^i(\underline{X}; \underline{\hat{u}}_i, \underline{\hat{u}}_{i+1}) = \underline{t}^i \cdot (\underline{\hat{u}}_{i+1} - \underline{\hat{u}}_i). \quad (107a)$$

Then, we have $\mathcal{L}_s^i(\underline{X}; \underline{u}_i, \underline{u}_{i+1}) = \dot{\ell}^i = d^i$ for any real motion.

The discrete strain rates for the twisting and bending modes are given by equations (100) and (104), respectively. Dependence of these strain rates on the velocities is captured by the following operators

$$\begin{aligned} \mathcal{L}_i^t(\underline{X}; \underline{\hat{u}}_{i-1}, \underline{\hat{u}}_i, \underline{\hat{u}}_{i+1}, \hat{v}^{i-1}, \hat{v}^i) \\ = \hat{v}^i - \hat{v}^{i-1} + \underline{K}_i \cdot \frac{\underline{\mathcal{V}}^{i-1}(\underline{X}; \underline{\hat{u}}_{i-1}, \underline{\hat{u}}_i) + \underline{\mathcal{V}}^i(\underline{X}; \underline{\hat{u}}_i, \underline{\hat{u}}_{i+1})}{2}. \end{aligned} \quad (107b)$$

and

$$\begin{aligned} \underline{\mathcal{L}}_i^b(\underline{X}; \underline{\hat{u}}_{i-1}, \underline{\hat{u}}_i, \underline{\hat{u}}_{i+1}, \hat{v}^{i-1}, \hat{v}^i) \\ = \underline{P}_\perp \left(\underline{\tilde{t}}_i, \mathcal{W}^i(\underline{X}; \underline{\hat{u}}_i, \underline{\hat{u}}_{i+1}, \hat{v}^i) - \mathcal{W}^{i-1}(\underline{X}; \underline{\hat{u}}_{i-1}, \underline{\hat{u}}_i, \hat{v}^{i-1}) \right). \end{aligned} \quad (107c)$$

For any real motion, \mathcal{L}_i^t and $\underline{\mathcal{L}}_i^b$ are equal to the strain rates $e_i^t = \dot{\tau}_i$ and \underline{e}_i^b , respectively. The definition \mathcal{L}_i^t makes use of the geometrical definition of discrete twist based on parallel transport.

5.9. Dissipation potentials

In our centerline/spin representation, the generalized velocity is a vector of dimension $4n + 7$ defined by collecting the linear velocities at the vertices, and the angular velocities of spin at the segments:

$$\underline{U}(t) = \{\underline{u}_0(t), v^0(t), \underline{u}_1(t), v^1(t), \dots, v^n(t), \underline{u}_{n+1}(t)\}. \quad (108)$$

This vector $\underline{U}(t)$ is the generalized velocity of the real motion. The dissipation potentials are defined in terms of arbitrary velocities, which we collect under the name of generalized virtual velocity $\underline{\hat{U}}$:

$$\underline{\hat{U}}(t) = \{\underline{\hat{u}}_0(t), \hat{v}^0(t), \underline{\hat{u}}_1(t), \hat{v}^1(t), \dots, \hat{v}^n(t), \underline{\hat{u}}_{n+1}(t)\}. \quad (109)$$

As in the smooth case, the viscous internal forces are introduced by means of dissipation potentials. The discrete potentials extend the smooth ones defined in equations (52):

$$\mathcal{D}_s(\underline{X}; \underline{\hat{U}}) = \frac{1}{2} \sum_{0 \leq i \leq n} D^i \left(\mathcal{L}_s^i(\underline{X}; \underline{\hat{u}}_i, \underline{\hat{u}}_{i+1}) \right)^2 \quad (110a)$$

$$\mathcal{D}_t(\underline{X}; \underline{\hat{U}}) = \frac{1}{2} \sum_{1 \leq i \leq n} C_i \left(\mathcal{L}_i^t(\underline{X}; \underline{\hat{u}}_{i-1}, \underline{\hat{u}}_i, \underline{\hat{u}}_{i+1}, \hat{v}^{i-1}, \hat{v}^i) \right)^2 \quad (110b)$$

$$\mathcal{D}_b(\underline{X}; \underline{\hat{U}}) = \frac{1}{2} \sum_{1 \leq i \leq n} B_i \left(\mathcal{L}_i^b(\underline{X}; \underline{\hat{u}}_{i-1}, \underline{\hat{u}}_i, \underline{\hat{u}}_{i+1}, \hat{v}^{i-1}, \hat{v}^i) \right)^2. \quad (110c)$$

Note that the stretching contribution involves a sum over all segments, although the twisting and bending contributions involve a sum over interior vertices. This is because the discrete axial strain d^i is defined on segments, while the strain rate vector \underline{e}_i relevant to the twisting and bending modes is defined on interior vertices.

In equations (110), the discrete moduli are defined by

$$D^i = \frac{3 \mu^i A^i}{\ell^i} \quad (111a)$$

$$C_i = \frac{2 [\widetilde{\mu I}]_i}{\tilde{\ell}_i} \quad (111b)$$

$$B_i = \frac{3 [\widetilde{\mu I}]_i}{\tilde{\ell}_i}. \quad (111c)$$

where μ^i is the fluid's dynamic viscosity which is stored at segments like other fluid properties, A^i is the segment's cross-sectional area reconstructed by equation (81), ℓ_i the segment length given by equation (74) and $\tilde{\ell}^i$ the length of the Voronoi cell around an interior vertices given by equation (82). The factor $[\widetilde{\mu I}]_i$ appearing the twisting and bending moduli is defined at vertices by linear interpolation over the adjacent segments:

$$[\widetilde{\mu I}]_i = \frac{1}{2} \frac{\mu^{i-1} (A^{i-1})^2 + \mu^i (A^i)^2}{4 \pi}. \quad (111d)$$

This definition is motivated by the fact that $I = A^2/(4\pi)$ in the smooth case, as shown by equation (22). Note that the discrete moduli satisfy the same relation $B_i/C_i = 3/2$ as in the smooth case; physically, this relation is a consequence of the fluid's incompressibility. All moduli depend on the actual configuration $\underline{X}(t)$ but not on velocities.

The definitions (111) of the discrete moduli are identical to the definitions (50) and (51) in the smooth setting, up to factors proportional to the discretization length ℓ^i or $\tilde{\ell}_i$. These factors were introduced so as to warrant convergence of the dissipation potentials in the smooth limit. For instance, for

the stretching contribution we have $D^i \sim \frac{D}{\ell^i}$, and $\mathcal{L}_s^i \sim \mathcal{L}_s \ell^i$ by equation (107a). Formal convergence of the corresponding dissipation potential follows:

$$\frac{1}{2} \sum_i D^i (\mathcal{L}_s^i)^2 \sim \frac{1}{2} \sum_i \frac{D}{\ell^i} (\mathcal{L}_s \ell^i)^2 \sim \frac{1}{2} \sum_i D (\mathcal{L}_s)^2 \ell^i \sim \frac{1}{2} \int_{S_-}^{S_+} D (\mathcal{L}_s)^2 dS \sim \mathcal{D}_s.$$

The total dissipation potential is defined by summing up the stretching, twisting and bending contributions:

$$\mathcal{D}(\underline{X}; \hat{\underline{U}}) = \mathcal{D}_s(\underline{X}; \hat{\underline{U}}) + \mathcal{D}_t(\underline{X}; \hat{\underline{U}}) + \mathcal{D}_b(\underline{X}; \hat{\underline{U}}). \quad (112)$$

5.10. Discrete equations of motion

The Rayleigh dissipation potential \mathcal{D} is used to derive the discrete viscous forces and moments. By analogy with equations (53a) and (53b), we model the internal viscous stress by a net force \underline{P}_i^v acting on the vertex \underline{x}_i , and by a twisting moment Q_v^i acting on the segment \underline{T}^i , both of which are given by a derivative of the dissipation potential:

$$\underline{P}_i^v(\underline{X}; \underline{U}) = - \left. \frac{\partial \mathcal{D}(\underline{X}; \hat{\underline{U}})}{\partial \hat{\underline{u}}_i} \right|_{\hat{\underline{U}} = \underline{U}} \quad (113a)$$

$$Q_v^i(\underline{X}; \underline{U}) = - \left. \frac{\partial \mathcal{D}(\underline{X}; \hat{\underline{U}})}{\partial \hat{v}^i} \right|_{\hat{\underline{U}} = \underline{U}} \quad (113b)$$

In these expressions, the partial derivative is with respect to the \underline{u}_i or \hat{v}^i entry inside the generalized coordinate vector $\hat{\underline{U}}$, see equation (109).

The discrete equations of motion read

$$\tilde{m}_i \dot{\underline{u}}_i(t) = \underline{P}_i^v(\underline{X}(t); \underline{U}(t)) + \underline{P}_i(t) \quad (114a)$$

$$\ell^i J^i \dot{v}^i(t) = Q_v^i(\underline{X}(t); \underline{U}(t)) + Q^i(t), \quad (114b)$$

where $\underline{P}_i(t)$ and $Q^i(t)$ define the external loading, \tilde{m}_i is the vertex-based mass, defined as the sum of half the mass of the segments adjacent to vertex \underline{x}_i ,

$$\tilde{m}_i = \sum_{j \in J_i} \frac{m^j}{2}, \quad (115a)$$

where the set of adjacent segments is $J_j = \{i-1, i\}$ if $0 < i < n+1$, $J_0 = \{0\}$ and $J_{n+1} = \{n\}$. Note that this vertex mass \tilde{m}_i could change over time if adaptation were used. In equation (114b), J^i is the density of moment of inertia of the cylinder attached to segment \underline{T}^i in actual configuration, per unit length:

$$J^i = 2\rho^i I^i = \frac{m^i}{V^i} \frac{(A^i)^2}{2\pi} \quad (115b)$$

and $\rho^i = m^i/V^i$ is the mass density of segment i .

The equations of motion can be written in compact form by introducing the generalized viscous force \underline{F}_v , the generalized external force \underline{F} and the mass matrix $\underline{\underline{M}}$. The latter are obtained by collecting vertex and segment-based components with the same ordering convention as in the generalized velocity \underline{U} :

$$\underline{F}_v = (\underline{P}_0^v, Q_v^0, \underline{P}_1^v, \dots, Q_v^n, \underline{P}_{n+1}^v) \quad (116a)$$

$$\underline{F} = (\underline{P}_0, Q^0, \underline{P}_1, \dots, Q^n, \underline{P}_{n+1}) \quad (116b)$$

$$\underline{\underline{M}} = \text{diag}(\tilde{m}_0 \underline{1}, \ell^0 J^0, \tilde{m}_1 \underline{1}, \dots, \ell^n J^n, \tilde{m}_{n+1} \underline{1}), \quad (116c)$$

where $\underline{1}$ represents the unit matrix in 3 dimensions. The equations of motion (114) and (113) can be rewritten as follows,

$$\underline{\underline{M}} \cdot \dot{\underline{U}}(t) = \underline{F}_v(\underline{X}(t), \underline{U}(t)) + \underline{F}(t) \quad (117a)$$

$$\underline{F}_v(\underline{X}, \underline{U}) = - \left. \frac{\partial \mathcal{D}(\underline{X}, \hat{\underline{U}})}{\partial \hat{\underline{U}}} \right|_{\hat{\underline{U}} = \underline{U}} \quad (117b)$$

$$\dot{\underline{X}}(t) = \underline{\underline{\Pi}}_n \cdot \underline{U}(t). \quad (117c)$$

The third equation is the definition of vertex velocities, $\underline{u}_i(t) = \dot{\underline{x}}_i(t)$. This equation makes use of the projection operator $\underline{\underline{\Pi}}_n$ mapping the degrees of freedom associated with vertices from the \underline{X} representation, from which segments are absent, to the \underline{U} representation:

$$\underline{\underline{\Pi}}_n = \sum_{i=0}^{n+1} \sum_{j=0}^2 \underline{\delta}_{3i+j} \otimes \underline{\delta}_{4i+j}. \quad (118)$$

Here $\underline{\underline{\Pi}}_n$ is a matrix of size $(3n+5) \times (4n+7)$, defined with the convention that vector indices start at 0. The index i runs over vertices, the index j over space directions, and $\underline{\delta}_k$ represents the vector whose entries are all 0, except for the k -th entry whose value is 1. The values $k = 3i + j$ and $k = 4i + j$ appearing in subscript are the indices of the degrees of freedom for vertex i in direction j in either representation.

Since the discrete dissipation potential is consistent in the smooth limit $n \rightarrow \infty$, the discrete viscous thread model converges to the smooth model in this limit: formally, the dynamical system in equations (117) becomes equivalent to the smooth equations of motion (55) combined with the expression (53) for the internal viscous forces. This convergence is checked numerically in section 8.

5.11. Surface tension and other forces

The weight of the thread is taken in account by setting $\underline{P}_i = \underline{g} \tilde{m}_i$ and $Q^i = 0$ in the equation of motion (116b). Here \tilde{m}_i is the mass attached to a vertex, defined in equation (115a), and \underline{g} the acceleration of gravity. In our validation experiments, the thread is formed by expelling fluid from a syringe, and letting it fall onto the ground under its own weight. The contact forces

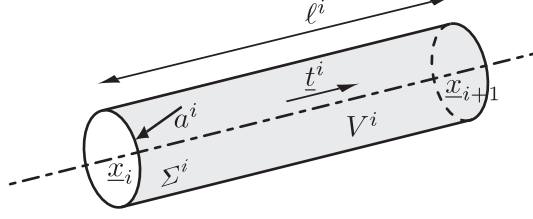


Figure 5: Surface tension is based on a cylindrical representation of the fluid attached to segments.

with the syringe or the ground need not be computed, as we treat contact using kinematical constraint and not penalty forces. This is explained in the forthcoming section 7.1.

We shall now explain how surface tension is taken into account — this is the last type of forces that we shall need in our examples. The present implementation of surface tension assumes that the segments are cylinders, as in figure 5. It is significantly simpler than that based on truncated cones presented in our conference paper [41]. The lateral area of the cylinder joining vertices \underline{x}_i and \underline{x}_{i+1} reads

$$\Sigma^i = 2\pi a^i \ell^i = 2\sqrt{\pi V^i \ell^i}, \quad (119)$$

as can be shown using $V^i = \pi (a^i)^2 \ell^i$. Its gradients with respect to the position of its endpoints read

$$\nabla_{\underline{x}_i} \Sigma^i = - \left(\frac{\pi V^i}{\ell^i} \right)^{1/2} \underline{t}^i = -\pi a^i \underline{t}^i \quad (120a)$$

$$\nabla_{\underline{x}_{i+1}} \Sigma^i = + \left(\frac{\pi V^i}{\ell^i} \right)^{1/2} \underline{t}^i = +\pi a^i \underline{t}^i. \quad (120b)$$

Here we have used $\nabla_{\underline{x}_i} \ell^i = \nabla_{\underline{x}_i} |\underline{x}_{i+1} - \underline{x}_i| = -\underline{t}^i$ and $\nabla_{\underline{x}_{i+1}} \ell^i = +\underline{t}^i$. Discrete surface tension forces are set up by means of the discrete capillary energy,

$$\mathcal{E}_\gamma(\underline{X}) = \sum_{i=0}^n \gamma^i \Sigma^i(\underline{X}). \quad (121)$$

Here γ^i is the fluid's surface tension at segment i . In this equation, we assume that the radius a^i of the cylinder varies over much longer length-scales than the radius itself, and neglect the longitudinal curvature of the lateral boundary in front of its azimuthal curvature. This is consistent with the thin thread approximation used everywhere in this paper. Let us note this approximation is not suited to the analysis of the Rayleigh-Taylor instability, whose critical wavelength is comparable to the radius. This instability would have to be studied using the full equations for 3D viscous fluids anyway, and not the dimensionally reduced equations for thin threads.

The expression for the discrete capillary forces at a vertex is given by minus the gradient of the capillary energy (121) with respect to vertex positions,

$$\underline{P}_i^\gamma = \begin{cases} +n_{\gamma t}^0 \underline{t}^0 & \text{if } i = 0 \\ -n_{\gamma t}^n \underline{t}^n & \text{if } i = n + 1 \\ +n_{\gamma t}^i \underline{t}^i - n_{\gamma t}^{i-1} \underline{t}^{i-1} & \text{if } 1 \leq i \leq n \end{cases} \quad (122a)$$

$$Q_\gamma^i = 0. \quad (122b)$$

The second equation is a consequence of the fact that the capillary energy depends only on vertex positions and not on the twist degree of freedom.

These vertex forces \underline{P}_i^γ are caused by an longitudinal force $n_{\gamma t}^i$, called the line tension, acting along each segment. Its magnitude is given by identification with equation (120),

$$n_{\gamma t}^i = \pi \gamma^i a^i. \quad (123)$$

This expression for the line tension $n_{\gamma t}^i$ can be interpreted as resulting from the overpressure in the fluid caused by the interface curvature $1/a^i$, according to the Young-Laplace law. As it derives from energy proportional to the lateral area, the capillary force tends to make the thread shorter and more compact, by bringing the endpoints closer to each other and by flattening out curved regions of the centerline.

The net capillary force on a vertex given in equation (122) has two contributions that almost cancel each other at each interior vertex (these contributions are associated with each one of the two adjacent segments), but only one contribution at the terminal vertices \underline{x}_0 and \underline{x}_{n+1} . This reflects the presence of Dirac contributions at the endpoints in the smooth model, see equation (60a). Note that the area of the cap closing the cylindrical thread near its endpoints is negligible, and the Dirac contributions are accurately captured even though these caps are not taken into account. Since the discrete model for surface tension has been derived from the energy in equation (121) which is a good approximation of the capillary energy in equation (59), the discrete capillary forces converge to the smooth ones in the limit $n \rightarrow \infty$. Our discrete model for surface tension is validated in section 8.3.

6. Time discretization, numerical implementation

6.1. Representation of the dissipation potential by a band matrix

The strain rate operators $\mathcal{L}_s^i(\underline{X}; \hat{\underline{U}})$, $\mathcal{L}_t^i(\underline{X}; \hat{\underline{U}})$ and $\mathcal{L}^b(\underline{X}; \hat{\underline{U}})$ defined in equations (107) are linear with respect to their virtual velocity argument $\hat{\underline{U}}$. The two first operators are real-valued: each one can be represented as a vector, denoted $\underline{\mathcal{L}}_s^i(\underline{X})$ or $\underline{\mathcal{L}}_t^i(\underline{X})$, that acts on $\hat{\underline{U}}$ by dot product. The last operator is vector-valued, and can be represented as a matrix $\underline{\underline{\mathcal{L}}}^b(\underline{X})$ acting on $\hat{\underline{U}}$:

$$\mathcal{L}_s^i(\underline{X}; \hat{\underline{U}}) = \underline{\mathcal{L}}_s^i(\underline{X}) \cdot \hat{\underline{U}} \quad (124a)$$

$$\mathcal{L}_t^i(\underline{X}; \hat{\underline{U}}) = \underline{\mathcal{L}}_t^i(\underline{X}) \cdot \hat{\underline{U}} \quad (124b)$$

$$\mathcal{L}^b(\underline{X}; \hat{\underline{U}}) = \underline{\underline{\mathcal{L}}}^b(\underline{X}) \cdot \hat{\underline{U}}. \quad (124c)$$

The tensors $\underline{\mathcal{L}}_s^i(\underline{X})$, $\underline{\mathcal{L}}_i^t(\underline{X})$ and $\underline{\mathcal{L}}_i^b(\underline{X})$ just introduced can be distinguished from the original functions as they bear one additional bar below, and have a single argument. They can be calculated explicitly (i) by setting the virtual velocity $\underline{\hat{U}} = \underline{\delta}_j$, i. e. by canceling all entries of $\underline{\hat{U}}$ except for the entry at index j which is set to one, (ii) by evaluating the left-hand sides above using the definitions (107), (iii) by filling the entry or column with index j in the target vector or matrix, and (iv) by iterating over the index j . In other words, we build the tensors using

$$\underline{\mathcal{L}}_s^i(\underline{X}) = \sum_{j=0}^{4n+6} \mathcal{L}_s^i(\underline{X}; \underline{\delta}_j) \otimes \underline{\delta}_j,$$

and similar formulas for $\underline{\mathcal{L}}_i^t(\underline{X})$ and $\underline{\mathcal{L}}_i^b(\underline{X})$.

Since the linear forms $\mathcal{L}_s^i(\underline{X}; \underline{\hat{U}})$, $\mathcal{L}_i^t(\underline{X}; \underline{\hat{U}})$ and $\mathcal{L}_i^b(\underline{X}; \underline{\hat{U}})$ attached to a segment or a vertex i depend only on the virtual velocities of the neighboring segments or vertices, the vectors and the matrix introduced in equations (124) are sparse. This sparse structure allows for efficient storage and manipulation.

Similarly, the dissipation potential is a quadratic function of the virtual velocity $\underline{\hat{U}}$. It can therefore be represented by a symmetric matrix $\underline{\mathcal{D}}(\underline{X})$, such that for any virtual velocity $\underline{\hat{U}}$

$$\mathcal{D}(\underline{X}; \underline{\hat{U}}) = \frac{1}{2} \underline{\hat{U}} \cdot \underline{\mathcal{D}}(\underline{X}) \cdot \underline{\hat{U}}. \quad (125)$$

This matrix is built up by combining the stretching, twisting and bending contributions,

$$\underline{\mathcal{D}}(\underline{X}) = \underline{\mathcal{D}}_s(\underline{X}) + \underline{\mathcal{D}}_t(\underline{X}) + \underline{\mathcal{D}}_b(\underline{X}). \quad (126)$$

Explicit formulae for these contributions can be found by inserting the representation of the linear operators in equations (124) into the definitions (110) of the discrete dissipation potentials:

$$\underline{\mathcal{D}}_s(\underline{X}) = \sum_{0 \leq i \leq n} D^i(\underline{X}) \underline{\mathcal{L}}_s^i(\underline{X}) \otimes \underline{\mathcal{L}}_s^i(\underline{X}) \quad (127a)$$

$$\underline{\mathcal{D}}_t(\underline{X}) = \sum_{1 \leq i \leq n} C_i(\underline{X}) \underline{\mathcal{L}}_i^t(\underline{X}) \otimes \underline{\mathcal{L}}_i^t(\underline{X}) \quad (127b)$$

$$\underline{\mathcal{D}}_b(\underline{X}) = \sum_{1 \leq i \leq n} B_i(\underline{X}) (\underline{\mathcal{L}}_i^b(\underline{X}))^T \cdot (\underline{\mathcal{L}}_i^b(\underline{X})). \quad (127c)$$

Because the linear forms in the right-hand sides are represented by sparse tensors, these symmetric matrices in the left-hand sides are all band-diagonal. Their band structure is shown in figure 6.

Note that new vertices are created during the simulation, while others collide with obstacles and are discarded. As a result, the number of vertices — and therefore the dimension of the dissipation matrix — may vary from one time step to the next.

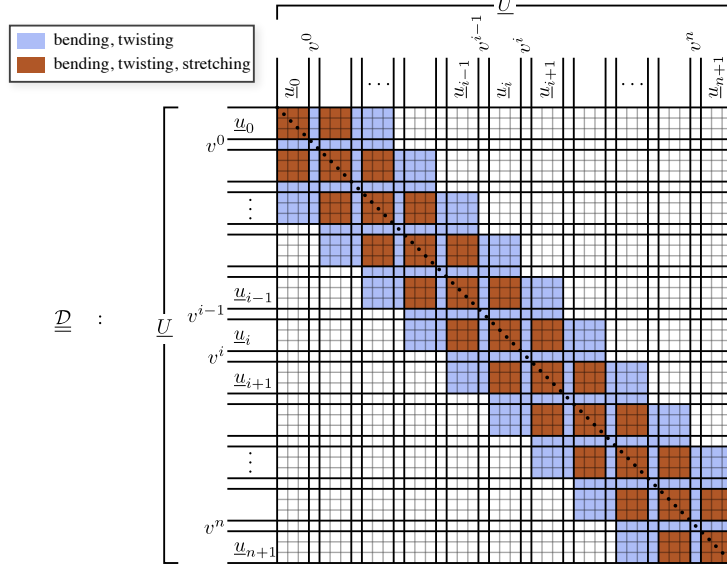


Figure 6: Band structure of the dissipation matrices $\underline{\underline{D}}_s(\underline{X})$, $\underline{\underline{D}}_t(\underline{X})$ and $\underline{\underline{D}}_b(\underline{X})$ for the stretching, twisting and bending modes.

6.2. Boundary conditions and kinematical constraints

We consider the possibility that some degrees of freedom are kinematically constrained. Such constraints are typically used to enforce boundary conditions. For instance, in the case of a clamped end, the velocities \underline{u}_0 and \underline{u}_1 of the first two vertices and the angular spinning velocity of the first segment v^0 are imposed by the motion of the clamp.

In the presence of kinematical constraints, the the generalized velocity $\underline{U}_{t+\epsilon}$ at the end of the time step is prescribed to be of the form

$$\underline{U}_{t+\epsilon} = \underline{\underline{B}} \cdot \underline{W}_{t+\epsilon} + \underline{B}', \quad (128)$$

where t is the time at the beginning of the time step, ϵ is the time step, and $\underline{W}_{t+\epsilon}$ is a reduced velocity vector collecting independent degrees of freedom. This vector $\underline{W}_{t+\epsilon}$ is the unknown of the time-stepping algorithm. Its size, denoted r , may vary from one time step to the next as constraints can be created or destroyed — this happens for instance when the thread makes its first contact with the ground.

The matrix $\underline{\underline{B}}$ is a $(4n+7) \times r$ matrix that dispatches the independent degrees of freedom into the generalized velocity vector \underline{U} . Given a strictly increasing numbering b of the unconstrained degrees of freedom, $b(0) < b(1) < \dots < b(r-1)$, this matrix reads

$$\underline{\underline{B}} = \sum_{i=0}^{r-1} \delta_{b(i)} \otimes \delta_i, \quad (129)$$

where $\underline{\delta}_j$ is the Dirac vector, $(\underline{\delta}_j)_i = 1$ for $i = j$, and 0 otherwise.

The last term in equation (128) is the vector \underline{B}' collecting the velocities of the constrained degrees of freedom in the final state $\underline{U}_{t+\epsilon}$. This vector is typically filled using the motion of the bodies in contact with the rod as explained in sections 7. Entries of \underline{B}' corresponding to unconstrained degrees of freedom can be set to zero by convention:

$$\underline{B}^T \cdot \underline{B}' = \underline{0}. \quad (130)$$

Indeed, allowing them to be non-zero would simply shift the value of the unknown $\underline{W}_{t+\epsilon}$.

As an illustration, consider the case when there is no kinematical constraints. Then $r = 4n+7$, $b(i) = i$ and $\underline{B}' = \underline{0}$, which implies that \underline{B} is the identity matrix. The more interesting case of a viscous thread, both ends of which are attached to clamps having a motion of pure translation with velocities $\underline{u}_{\text{clamp}}^1$ and $\underline{u}_{\text{clamp}}^2$ is handled by setting

$$r = 4n + 7 - 2 \times 7 = 4n - 7 \quad (131a)$$

$$b(i) = i - 7 \quad (131b)$$

$$\underline{B}' = (\underline{u}_{\text{clamp}}^1, 0, \underline{u}_{\text{clamp}}^1, 0, \underline{0}, \dots, \underline{0}, 0, \underline{u}_{\text{clamp}}^2, 0, \underline{u}_{\text{clamp}}^2). \quad (131c)$$

In the presence of kinematical constraints, we discard the equations of motion corresponding to the constrained degrees of freedom. This is achieved by left-multiplying both sides of equation (117a) by \underline{B}^T , and the equation of motion becomes

$$\underline{B}^T \cdot \underline{M} \cdot \dot{\underline{U}}(t) = \underline{B}^T \cdot \left(\underline{F}_v(\underline{X}(t), \underline{U}(t)) + \underline{F}(t) \right). \quad (132)$$

6.3. Time discretization and time-stepping

The time step ϵ can be fixed or variable. At each time step, the updated position $\underline{X}_{t+\epsilon}$ and velocity $\underline{U}_{t+\epsilon}$ must be determined from the actual position \underline{X}_t and velocity \underline{U}_t . We discretize equation (132) in time using a linear implicit scheme. The viscous force \underline{F}_v is evaluated implicitly with respect velocity but explicitly with respect to position:

$$\underline{B}^T \cdot \underline{M} \cdot \frac{\underline{U}_{t+\epsilon} - \underline{U}_t}{\epsilon} = \underline{B}^T \cdot \left(\underline{F}_v(\underline{X}_t, \underline{U}_{t+\epsilon}) + \underline{F}(t) \right). \quad (133)$$

This choice combines good stability, as demonstrated by the validation examples, and ease of implementation: only a linear solver is required.

The viscous force $\underline{F}_v(\underline{X}_t, \underline{U}_{t+\epsilon})$ is indeed linear with respect to the unknown $\underline{U}_{t+\epsilon}$ by equations (117b) and (125),

$$\underline{F}_v(\underline{X}; \underline{U}) = -\frac{\partial \mathcal{D}}{\partial \underline{U}} = -\underline{\mathcal{D}}(\underline{X}) \cdot \underline{U}. \quad (134)$$

Inserting equations (128) and (134) into the equation of motion (132), we find that the update rule for the velocity takes the form of a linear equation to be

solved for $\underline{W}_{t+\epsilon}$:

$$\left[\underline{\underline{B}}^T \cdot (\underline{\underline{M}} + \epsilon \underline{\underline{D}}(\underline{X}_t)) \cdot \underline{\underline{B}} \right] \cdot \underline{W}_{t+\epsilon} = \underline{\underline{B}}^T \cdot (\epsilon (-\underline{\underline{D}}(\underline{X}_t) \cdot \underline{B}' + \underline{F}(t)) - \underline{\underline{M}} \cdot (\underline{B}' - \underline{U}_t)). \quad (135)$$

In this equation, $\underline{\underline{B}}$ and \underline{B}' encode kinematical constraints, $\underline{\underline{M}}$ is the mass matrix, $\underline{\underline{D}}$ the viscous dissipation matrix representing internal stress, $\underline{F}(t)$ is the external loading and \underline{U}_t the velocity at the start of the time step. The matrix in square brackets in the left-hand side is symmetric, positive definite for any value of the time increment $\epsilon > 0$. As a result, this linear equation can be solved using efficient and robust solvers.

Note that the external force $\underline{F}(t)$, which includes in particular the effect of capillary forces, is evaluated explicitly. We have tried a linear implicit implementation of surface tension, but have not observed any significant improvement in stability: an explicit evaluation of surface tension force does not raise any stability issue in all our tests.

Once the linear equation for $\underline{W}_{t+\epsilon}$ has been solved, the generalized velocity $\underline{U}_{t+\epsilon}$ is reconstructed by means of equation (128). Positions are then incremented using a discrete version of equation (117c),

$$\underline{X}_{t+\epsilon} = \underline{X}_t + \underline{\Pi}_n \cdot \underline{U}_{t+\epsilon}. \quad (136)$$

6.4. Time-stepping: summary

The main task of the time stepping loop is to set up and solve equation (135). Algorithm 1 explains how the various quantities appearing in this equation are constructed, and provide an overview of the implementation of the time step.

Require: ϵ {time step}
Require: m^i, V^i, μ^i {fluid properties}
Require: $\underline{x}_i(t), \underline{u}_i(t), v^i(t)$ {initial positions and velocities}
Require: $\underline{\underline{B}}, \underline{B}'$ {kinematical constraints at boundaries, §6.2 §7}
Require: \underline{F}_T {external force, §5.11 and eq. (116b)}
 1: set ℓ^i, A^i and $\tilde{\ell}_i$ {geometry, §5.1 and §5.2}
 2: set D^i, C_i, B_i {viscous moduli, eq. (111)}
 3: set $\underline{\underline{L}}_s^i, \underline{\underline{L}}_i^t, \underline{\underline{L}}_i^b$ {discrete strain rates, §5.8 and §6.1}
 4: set $\underline{\underline{D}}$ {dissipation matrix, eqs. (126–127)}
 5: assemble \underline{X}_t and \underline{U}_t {eqs. (105) and (108)}
 6: set \tilde{m}_i and J^i {eqs. (115) and/or (137)}
 7: assemble $\underline{\underline{M}}$ {eq. (116c)}
 8: solve for $\underline{W}_{t+\epsilon}$ {eq. (135)}
 9: reconstruct $\underline{U}_{t+\epsilon}$ {eq. (128)}
 10: update $\underline{u}_i(t + \epsilon), v^i(t + \epsilon)$ {eq. (108)}
 11: update $\underline{x}_i(t + \epsilon)$ {eq. (136)}

Algorithm 1: Overview of a time step.

Note that fluid properties such as the mass m^j , volume V^j and viscosity μ^j are stored in segments. These properties are constant in most of the examples

shown here. They may however depend on time, either when adaptation is used (see section 6.5), or when the dynamics of the thread is coupled to another physical process, as for instance in the case of heat transfer and temperature-dependent viscosity — a separate update rule is then required. In addition segments store their spinning velocity v^j .

By the argument of section 3.13, rotational inertia can be neglected for a thin thread. In all the examples shown here, the rotational inertia was set to zero,

$$J^j = 0. \quad (137)$$

We have compared simulations done using this approximation with simulations based on the exact value of J^j given in equation (115b), and checked that the results are indeed very close when the thread’s radius is small.

6.5. Adaptive mesh refinement

In the the experiments of Morris [13], which we reproduce in section 9.2, gravity stretches the thread by a factor which can be as large as 10 to 100. In the absence of refinement, the segments in the bottom part of the thread would be considerably longer than those at the top. A good spatial resolution is needed at the bottom, where the impact with the hard surface forms a coils of small radius. This makes simulations of severely stretched threads extremely inefficient, unless spatial refinement is used.

We have implemented adaptive mesh refinement as follows. At the end of every dynamic step detailed in algorithm 1, the segments needing refinement are first marked according to some user-defined criterion; next, segments that have been marked are actually split: a new vertex is inserted in each segment undergoing subdivision, and quantities such as mass, radius, position, velocity etc. are calculated in the new vertices and segments, as explained below. The refined thread is then used as the initial state for the next dynamic step.

The refinement criterion can be based on comparing length of the segment to a maximum prescribed length. Other criteria based on the turning angle with respect to the neighboring segments have been considered too, but not used in the examples. The maximum allowed length may be a function of the position of the midpoint of the segment, to force refinement near a boundary for instance. In each case, the refinement criterion was adjusted manually to offer the best compromise between efficiency and accuracy — even if introduced in the context of non-steady problems such as the viscous sewing machine, refinement was always first validated in a steady coiling geometry, as explained in section 8.

Whenever a segment has been marked, its subdivision is carried out as follows. A new vertex is inserted, two new segments are allocated and the former segment is removed. The position \underline{x}_i and velocity \underline{u}_i of the new vertex are calculated by an interpolation of order 4 based on the positions and velocities of its neighboring vertices. Vertices resulting from a subdivision concomitant with that under consideration do not enter in this interpolation, and so the result is independent of the order in which marked segments are processed. The mass m^j stored in the original segment is equally split among the two subsegments. The

viscosity μ^j , surface tension γ^j , spinning velocity v^j of the new subsegments are all computed by an interpolation of order 2 based on the values of the former segment and of its neighbors. Finally, the volume V^j of the subsegments is computed by first considering an interpolation of the cross-sectional area A^i at order 4, which is then multiplied by the length of the subsegment. This procedure and the interpolation orders have been chosen in such a way that the viscous twisting and bending forces, which depend on the derivatives of order up to four of the positions, remain smooth upon subdivision.

7. Interaction of the thread with other bodies

Interaction with two types of rigid bodies are considered in our validation examples: a fluid container, such as a syringe, delivering fluid at a fixed volume rate, and a rigid impenetrable surface onto which the thread impinges. The interaction is taken care of using kinematical constraints. The vertices that have not yet been pushed outside the container, as well as those that have collided with the surface, are constrained. Their positions and velocities are prescribed by the motion of the body. In this section, we explain how the matrix \underline{B} and the vector \underline{B}' , which represent these constraints in algorithm 1, are calculated. For the sake of simplicity, we assume that the motion of the external bodies is unaffected by the motion of the thread; two-way coupling with external bodies could be enforced as a kinematical constraint, and would typically be handled by a post-integration step using a manifold projection method [75].

7.1. Fluid container

In the experiments, the viscous fluid is fed from a container at a constant volume rate Q_c through a circular opening of diameter d_c by a syringe controlled by a step motor, see figure 7a. Let $A_c = \pi \frac{d_c^2}{4}$ be the area of the opening. The imposed volume rate sets an ejection velocity $U_c = Q_c/A_c$ of the thread relative to the container. The velocity of the fluid exiting from the container is the sum of the prescribed velocity of the container, and this relative velocity U_c .

At the exit from the container, the thread is clamped, *i. e.* the centerline position, tangent, and the rotation are all prescribed. This clamped boundary condition is implemented by blocking the rotation of the segment joining the first two vertices, and constraining the positions of these two vertices (this has the effect of blocking the unit tangent vector parallel to the first segment). These kinematical constraints are implemented as explained in section (6.2). Clamped boundary conditions therefore require that two vertices lie inside the container at all times.

7.1.1. Simple container model

A simple discrete model for the container is sketched in figure 7b. The two topmost vertices of the thread are located inside the container and move with the velocity $-U_c \underline{e}_z$ relative to the container. Here \underline{e}_z is the unit vector, usually vertical, which is opposite to the direction of ejection. At every time step,

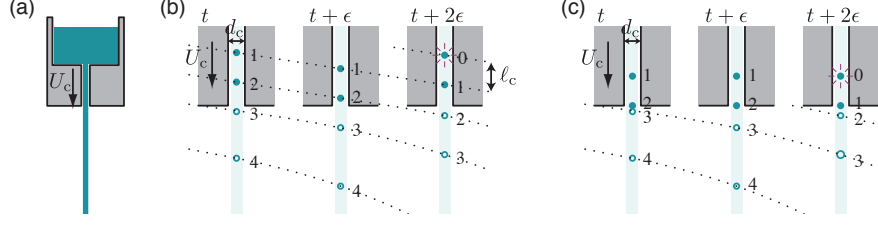


Figure 7: Discrete representation of the container delivering fluid through a circular opening of diameter d_c at a prescribed vertical velocity U_c , shown in (a). Clamped boundary conditions are enforced by prescribing the position and velocities of the two topmost vertices, and blocking the rotation of the first segment joining them. Filled disks represent constrained vertices (top part of the thread attached to the container), open circles represents unconstrained vertices (hanging part of the thread), dashed curves are the timelines of vertices. (b) Simple implementation whereby the two first vertices move with prescribed vertical velocity U_c . (c) In a refined implementation, the first two vertices are kept at a fixed position with respect to the container, and mass is continuously added into the second segment. In both cases (b) and (c) a new vertex is periodically created from top (vertex labelled ‘0’ appearing at time $t + 2\epsilon$), and there are always two vertices inside the container.

whenever one of these two vertices goes past the opening of the container, it is freed (its position constraint is discarded) and a new constrained vertex is added on top of the thread, as happens in frame $t + 2\epsilon$ in figure 7b; the new segment on top is assigned a length ℓ_c , a volume ($A_c \ell_c$), a mass ($\rho A_c \ell_c$), and surface tension γ . Here, ρ and γ are the mass density and surface tension of the fluid in the container, and the length ℓ_c is a discretization parameter chosen by the user.

This simple implementation has a drawback: it induces oscillations of the thread with a small amplitude and a large frequency. Indeed the effective fall height is determined by the position of the second topmost vertex. As a function of time, this height varies abruptly every time a new vertex is added. The amplitude of the discontinuity is set by the spacing between vertices in the containers. We found that this small-amplitude, large-frequency forcing usually allowed convergence of positions and velocities with finer and finer discretization lengths ℓ_c , but induces unbounded fluctuations of acceleration.

7.1.2. Refined container model

We found it necessary to suppress the oscillations to obtain convergent and fully reproducible results, and to capture the subtle patterns produced by the viscous sewing machine at large fall heights [76]. To do so, we used an improved description of the container which is sketched in figure 7c. The first two vertices do not follow fluid particles but instead stay at a fixed position with respect to the container. As earlier, their velocity is constrained to the value $-U_c \underline{e}_z$ relative to the container at the start of each dynamic step, but their position is systematically reset after each dynamic step, so as to make the second vertex coincide with the opening of the container and the first vertex lie at distance ℓ_c above it. At each time step ϵ , an incremental volume of fluid (ϵQ_c) and the

associated mass ($\rho \epsilon Q_c$) provided by the container are assigned to the *second* segment. Whenever its volume exceeds the target value ($A_c \ell_c$) fixed by the discretization parameter ℓ_c , this segment is split, a new vertex is inserted between the second and third vertices; the fluid material in excess is then assigned to the new segment, as sketched in figure 7c. In this improved implementation of the boundary conditions, the fall height varies smoothly as a function of time. We found that this was sufficient to make the acceleration converge smoothly in the limit of a fine discretization, and produce stitching patterns that are both reproducible and consistent with the sewing machine experiments. All examples shown in Sections 8 and 9 make use of this refined model.

7.2. *Collisions on a hard surface*

We now consider collisions with a rigid obstacle. When the thread hits the obstacle, it sticks to it and gets carried away by the obstacle. The obstacle may be at rest, as in the case of steady coiling of section 8, or in motion, as happens with the moving belt in the sewing machine experiment of section 9.2. In the latter case, the motion of the obstacle is prescribed. Detection of collisions involves comparing the distance of vertices to the obstacle, to the radius a^i of the adjacent segments defined in equation (81).

7.2.1. *‘Capture and continue’ mode*

In a straightforward implementation, called the ‘capture and continue’ mode, we detect collisions with the obstacle at the end of every dynamic step, and mark the colliding vertices as being captured: in all subsequent dynamic steps, their positions and velocities are constrained based on the motion of the obstacle and on their relative position to the obstacle when they were captured. Slip-free conditions are considered: the rotation of segments joining any pair of captured vertices is blocked as well. We found that this simple description of the collisions was another source of large, spurious fluctuations in acceleration. The oscillations can be interpreted by the fact that the vertical momentum resulting from a collision is not transferred to the thread until the following time step, when the position constraints take effect. Another drawback of the method, which is partly responsible for oscillations, is that the thread penetrates into the obstacle by a small but very irregular depth, roughly proportional to the time step duration.

7.2.2. *‘Time roll-back’ mode*

The oscillations were removed by using a *roll-back*, which allows for a more accurate handling of collisions. A roll-back discards any dynamic time step ending up in unexpected collisions. The time step is recomputed with the motion of the colliding vertices constrained in such a way that they come exactly in contact with the obstacle at the end of the time step. Roll-back can be viewed as an iterative predictor-corrector or iterative constraint refinement method [77]: a new unexpected collision may take place during the second tentative time step, inducing a third attempt, etc. A list of expected collisions is kept and updated after unsuccessful time step.

Roll-back removes the two main limitations of the straightforward ‘capture and continue’ implementation: it suppresses the delay in transferring momentum from the obstacle to the thread, and makes the thread land exactly at the surface of the obstacle, removing the unwanted rugosity produced by the ‘capture and continue’ mode. We found that roll-back does indeed suppress the spurious oscillations very effectively, bringing about benefits similar to those of the improved nozzle implementation discussed in section 7.1.2. All the validation examples shown in the following sections make use of the time roll-back method.

If many collisions occur during a single time step, the roll-back method does not work well and spurious fluctuations reemerge in the acceleration as a function of time. The reason is that we work in the context of a linearized implicit scheme, in which the equations of motion are always linearized using the solution at the start of the time step. The successive iterations of a given time step all start from the same configurations. As a result, they all make use of the same set of linearized equations. If too many collisions occur before the end of the time step, this linearization becomes a poor approximation of the actual motion. To work around this limitation, we combined roll-back with time adaptation: if a new collision is detected before the end of the tentative time step, the next tentative time step is shortened and scheduled to end at the collision time estimated from the previous iteration. This time adaptation reduces the time step dynamically, in such a way that there is at most one collision per time step. The drawback is the increased complexity in implementation, and the fact that the simulation time increases with the rate of collisions.

8. Validation in a steady coiling geometry

We proceed to validate our discrete model and verify our implementation, by checking convergence in the smooth limit. We consider the steady coiling motion of a viscous thread stretched by gravity and impinging on a surface at rest, as shown in figure 8b. Our simulation results are compared to reference solutions kindly provided by N. Ribe, which are based on numerical continuation of the time-independent problem expressed in the co-rotating frame [9], and solved using the AUTO software [78].

8.1. Validation of bending, stretching, gravity, inertia and collisions

The following set of parameters are used for validation and verification: the fluid’s dynamical viscosity $\mu = 0.2$ and mass density $\rho = 5 \cdot 10^{-4}$, the acceleration of gravity $g = 9.81$, the area $A_c = 6.44 \cdot 10^{-3}$ of the circular outlet of the container and the fluid’s volume rate $Q_c = 3.96 \cdot 10^{-3}$. The surface tension γ is set to zero until we validate surface tension later in section 8.3.

Three dimensionless groups characterize the properties of the fluid and the container [11]:

$$\Pi_1 = \left(\frac{\nu^5}{g Q_c^3} \right)^{1/5}, \quad \Pi_2 = \left(\frac{\nu Q_c}{g d_c^4} \right)^{1/4}, \quad \Pi_3 = \frac{d_c^2 \gamma}{Q_c \mu}, \quad (138)$$

where $\nu = \mu/\rho$ is the kinematical viscosity; the diameter of the container's circular opening d_c and the extrusion velocity $U_c = Q_c/A_c$ have been defined in section 7.1. The numerical values of the dimensionless groups are $\Pi_1 = 7000$, $\Pi_2 = 7$ and $\Pi_3 = 0$ for the set of parameters listed above. This corresponds to significant, but not extreme, stretching: the radius decreases by a factor of order 2 during the course of the descent for the range of heights considered below.

Based on the acceleration of gravity g and on the kinematical viscosity ν , one can define a natural length scale L^* and a natural time scale T^* by

$$L^* = \left(\frac{\nu^2}{g}\right)^{1/3}, \quad T^* = \left(\frac{\nu}{g^2}\right)^{1/3}. \quad (139)$$

Numerically, $L^* = 25.36$ and $T^* = 1.61$ using the above set of parameters. These scales are used to make the simulation results dimensionless when comparing to the reference solution.

Two additional discretization parameters are needed in the simulation: the initial segment length ℓ_c , introduced in section 7.1, and the time step ϵ . Unless otherwise specified, their values are set to $\ell_c = 0.025$ and $\epsilon = 0.02$. Note that the average number of particles emitted per time step is $(\epsilon U_c/\ell_c) = 0.49$. A good trade-off between accuracy and efficiency requires that this number is neither very small nor very large.

The reference solution of N. Ribe [9] takes the form of data for the coiling radius or the coiling frequency, as a function of the fall height. To produce simulation data which can be compared to this reference solution, a range of fall heights $H(t)$ is swept in a single simulation run. To this end, the motion of the container is prescribed in a sequence of up to three phases in our simulations. At initial time $t = 0$, it is placed at height H_0 . It is left still until time $t = t_1$, when the steady coiling is established. Then, the container is moved upwards at a prescribed velocity V_c that is much smaller than the extrusion velocity U_c , until time $t = t_2$. In a last phase, from time $t = t_2$ to the end of the simulation, $t = t_f$, the container is moved slowly downwards at the same velocity V_c . Unless otherwise specified, we set $t_1 = 30$, $t_2 = 1530$, $t_f = 3030$ and $V_c = 0.02$, which is 30 times slower than the extrusion velocity.

Validation results are shown in figure 8. Most of the time, the simulation lays down a thin curve (brown and blue) in the plane (H, R) , where $R = (x^2 + y^2)^{1/2}$ is the distance of the point of contact of the thread with the floor, to the axis passing through the nozzle. This indicates a steady coiling regime. When the container is moved up (brown curve), the simulated radius R follows closely the reference solution, until the latter folds back onto itself. The portion of the reference curve immediately past the fold point is known to be unstable [11]. The simulation then goes to a transient regime, labeled 'C' in figure 8a and shown in figure 11. It then settles to a different branch of solutions having a smaller radius. A series of such bifurcations is observed in the simulation, a behavior that has been observed in experiments too [11]. A similar sequence of transitions is observed when the container is moved down. As multiple coiling solutions are in competition, a hysteretic behavior is observed: transition from

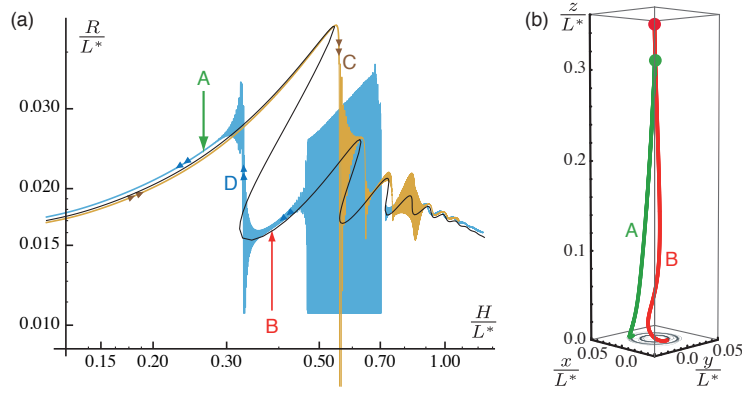


Figure 8: Validation in a steady coiling geometry, with $\Pi_1 = 7000$, $\Pi_2 = 7$ and $\Pi_3 = 0$ (no surface tension). (a) The coiling radius $R = (x^2 + y^2)^{1/2}$ is recorded continuously as the fall height H is varied, by slowly moving the container upwards (brown curve) and then downwards (blue curve). It is compared against the reference solution of N. Ribe obtained by numerical continuation (black), after rescaling by the length scale L^* . Note the abrupt changes in the coiling radius at places where the reference solution folds back onto itself, as expected. Filled regions correspond to a rapidly varying radius, either because the thread goes to a steady folding mode, as happens around $H = .60$, or because of a transient regime following a branch jump. (b) Two typical configurations of the thread, for different fall heights. Note that the fundamental mode of a hanging viscous string is excited in ‘A’, while its first harmonic is excited in ‘B’: the red curve has a node near $z/L^* = .05$.

the branch corresponding to the largest coiling radius to the second largest occurs at a height ‘C’ when the container moves up, which is larger than the transition height ‘D’ observed on the way back. We observe the occurrence of a folding mode in the interval $.72 > H/L^* > .47$ when the container moves down, but will not comment further on it as little is known on the competition between the coiling and folding modes. The small gap between the blue and brown curves in the left part of figure 8a can be attributed to the fact that the velocity of the container V_c is small but finite. Overall, the simulation is in good agreement with the reference curve, and reproduces the details of its meandering shape. This validates the various physical ingredients that affect the reference curve, namely viscous bending and stretching, gravity, inertia and contact with the floor.

A detailed run such as the one shown in figure 8, corresponding to a total simulation time $t_f = 3030$ and a total number of time steps $t_f/\epsilon \approx 150 \cdot 10^3$, runs in about 30 min on a 2.6 Ghz Intel Core i7 processor using 8 GB of memory. The maximum number of vertices, when the fall height is maximum, is 460, corresponding to approximately 1800 degrees of freedom.

8.2. Analysis of convergence

Convergence of the solution towards the reference solution of N. Ribe is shown in figure 9 as a function of the discretization parameters. Convergence is

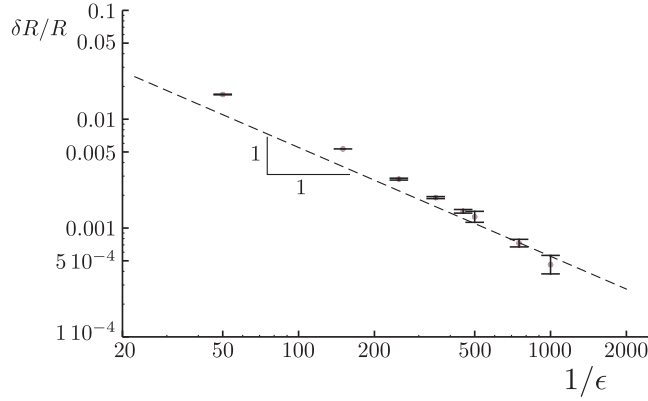


Figure 9: Analysis of convergence towards the reference solution in steady coiling geometry, showing the relative error on the coiling radius $\delta R/R$ as a function of mesh size and time step. The same parameters are used as in figure 8, but the time step and the discretization length are varied in the intervals $.02 \leq \epsilon \leq .2$ and $.025 \leq \ell_c \leq .25$, their ratio being kept constant. Fall height is fixed to $H = 1.01$.

challenging in the presence of collisions on the floor, and we found it necessary to use the refined models for the floor and container described in sections 7.1.2 and 7.2.2. In our simulation the coiling radius R is measured after a time that is long enough for the initial transient to disappear, and then averaged over several periods. The simulation is repeated for different values of the time step ϵ and discretization length ℓ_c , their ratio being kept constant. Convergence of our numerical method is confirmed by the fact that the residual error goes to zero. The convergence appears to be linear with the discretization parameters.

8.3. Validation of surface tension

With the aim to validate our discrete model for surface tension, we repeat the validation shown in figure 8 using the same set of parameters, except for the surface tension coefficient, now set to $\gamma = 10^{-3}$. The corresponding dimensionless parameter is $\Pi_3 = 10.3 \cdot 10^{-3}$. Surface tension has a marked effect on the coiling radius, as shown by comparison of the solid and dashed black curves in figure 10. We obtain a good agreement between the simulation and the new reference curve. This validates our discrete surface tension model.

9. Discussion

9.1. Transient regimes

Even though the steady coiling geometry provides a convenient set-up for validation and verification, our numerical method can solve the non-steady dynamics of viscous threads. As an illustration, transient regimes following jumps from one branch of steady coiling solutions to the next are shown in figure 11.

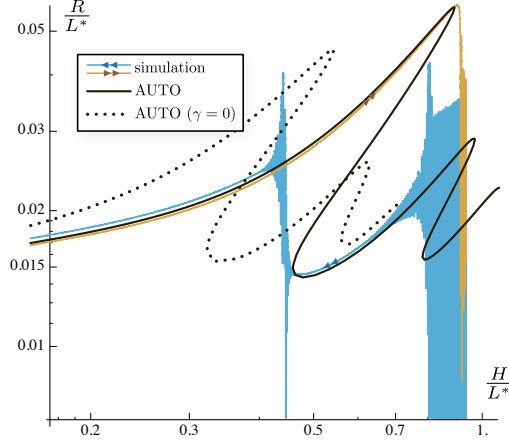


Figure 10: Validation of surface tension using steady coiling ($\Pi_1 = 7000$, $\Pi_2 = 7$, $\Pi_3 = 10.3 \cdot 10^{-3}$). The same parameters are used as in figure 8, except for the non-zero surface tension $\gamma = 10^{-3}$. A good agreement is obtained with the reference curve that takes into account surface tension (solid black curve). For reference, the reference solution with zero surface tension is shown (dotted curve).

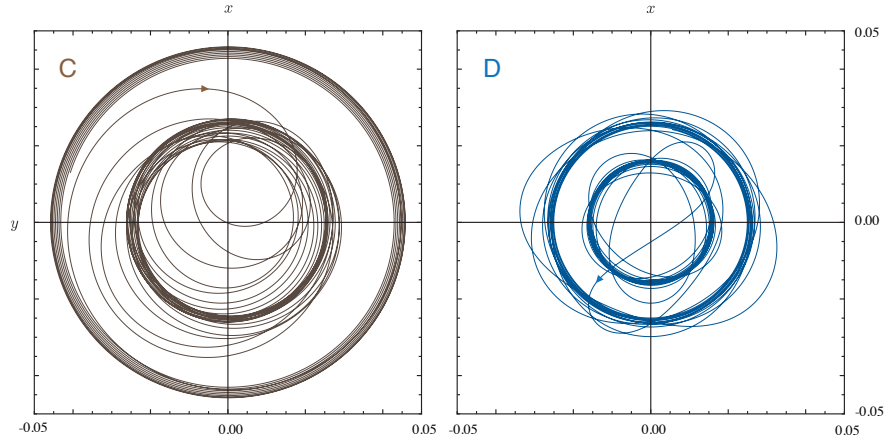


Figure 11: Trace laid out by the thread in the simulation, in the transient regimes following the jumps labelled 'C' and 'D' in figure 8. In 'C', the fall height is slowly increased and the thread jumps to a solution having a smaller radius; in 'D', the fall height is slowly decreased, and the thread jumps to a solution having a larger radius. Same simulation parameters as in figure 8.



Figure 12: Simulation of the so-called numerical sewing machine. The thread is poured from a constant height onto a moving belt. As the velocity of the belt is increased, the pattern laid out by the thread undergoes a series of bifurcations, similar to those that have been reported in the experiments: for this particular value of the fall height, translated coiling, alternated loops and meanders are successively obtained. Arrows indicate the velocity of the belt as the pattern was formed: the belt moves to the right and more ancient patterns, corresponding to a slower belt, are located on the right hand side. Simulation parameters are the same as in reference [13] and are provided in main text.

9.2. The viscous sewing machine

The fluid-mechanical sewing machine is an extension of the steady coiling problem to the case of a moving substrate. To the best of our knowledge, our numerical method is the first one that can simulate this non-steady phenomenon. In fact the possibility to set up numerical simulations of the experiments described in references [12, 13] acted as an incentive for us to develop the present simulation method.

A numerical investigation of the fluid-mechanical sewing machine is the topic of a separate detailed paper [76]. In figure 12, a simple demonstration run is presented. In this simulation, the velocity of the belt is steadily increased. The patterns must be read from right to left: this corresponds to the order in which they were produced, and so to an increasing belt velocities. On the right-hand side, for a low belt velocity, the translated coiling pattern is obtained. Increasing the belt velocity, two successive transitions are observed, leading to the formation of alternated loops first, and to meanders next. For even larger belt velocities, the oscillations disappear and the pattern becomes straight (not shown) as the hanging part of the thread takes on a catenary-like shape. The same sequence of patterns has been observed in the experiments, and is typical of small fall heights. A variety of patterns, some of which are quite complex, are obtained at larger fall heights both in the experiments and in the simulations, see reference [76] for details.

The parameters used to produce the results of figure 12 are the same as in the experiments of Morris [13]. We use a convenient set of units in which the fluid's dynamical viscosity is $\mu = 1$, its mass density is $\rho = 1$, and the acceleration of gravity is $g = 1$. With this natural set of units, the quantities L^* and T^* defined earlier read $L^* = 1$ and $T^* = 1$. The fall height is fixed to $H = 0.865$; this corresponds to a physical fall height of 3.7 cm in the experiments [13]. The area of the circular outlet at the bottom of the container is set to $A_c = 0.0275$, and the imposed volume flow rate is $Q_c = 2.29 \cdot 10^{-5}$, and there is no surface tension, $\gamma = 0$. The corresponding values of the dimensionless groups read $\Pi_1 = 608.5$, $\Pi_2 = 0.369$, $\Pi_3 = 0$. The spatial discretization parameter is set to $\ell_c = 0.005$, and the temporal one to $\epsilon = 0.05$. The stretching effect of gravity is severe, and the mesh is refined adaptively to maintain a good resolution near the

bottom of the thread while keeping a reasonable number of degrees of freedom, as explained in section 6.5: a given segment is refined up to six times in the simulation. The belt is held still until time $t_1 = 919$ to the initial transient relax. From this time on, the belt velocity is steadily accelerated until the end of the simulation, occurring at time $t_f = 1650$, its final velocity being 0.02.

9.3. Limitations and perspective

For the simulation results to be reproducible, we found it critical to fine-tune the discretization parameters in a steady coiling geometry, before attempting to simulate non-steady behaviors. Checking the convergence of positions, typically by comparing the coiling radius to the reference solution, appeared not to be sufficient. We had to suppress any fast residual oscillation in the computed acceleration, by using the refined description of obstacles described in section 7, and by carefully choosing the discretization parameters.

The present paper presents a linear implicit scheme: at each time step, the velocity is updated using a linear expression for the viscous forces, which is accurate in the vicinity of the previous configuration, see equations (126–127) and (135); the position is then updated separately using this velocity, see equation (136). Compared to an explicit scheme, this method is more difficult to implement but vastly superior in terms of stability. In a previous paper, we have explored a fully implicit scheme [41], by retaining the non-linear dependence of the viscous forces on positions: in that case, each time step requires a non-linear root-finding. The benefit of the non-linear implicit approach is that it preserves conservation laws associated with the symmetries of the problem, such as the conservation of the angular momentum, when it applies. By contrast the method presented here displays the usual dissipation of angular momentum. This is a minor drawback as viscous thread are rarely free-standing in practical applications. In all the demonstration examples shown earlier, neither the linear nor the angular momentum of the thread are actually conserved, because of the contact forces with the floor.

Simulations of viscous threads and elastic rods can be unified [41]: in that treatment all the code is shared by both rods and threads, except that in the viscous case the undeformed configuration is updated at each time step. This makes the combined approach very appealing. Nevertheless, a benefit of the specialized implementation presented here is that it saves the burden of implementing the Hessian matrix for naturally curved elastic rods.

In future work, it would be interesting to extend the present numerical model to thin threads governed by more general constitutive laws, such as visco-elastic filaments [49, 79] which can exhibit a complex and poorly understood behavior [80]. To this end, the discrete geometrical model exposed in the present paper can be reused and combined with different constitutive laws. It would also be interesting to couple our thin thread model with existing simulation methods for 3D flows with free boundaries [81, 82, 20, 72], in order to capture the interaction of the thread with the slowly collapsing pile that forms where it merges with the bath.

9.4. Conclusion

We have presented a numerical method for simulating the dynamics of thin viscous threads. In contrast with existing numerical methods, it captures the combined effects of stretching, bending and twisting forces, inertia and large rotations. It is not restricted to steady flows. The method has been derived by writing the smooth equations of motion for thin threads into a Lagrangian form, and using a careful spatial discretization. In particular, a discrete notion of twist has been used, which is based on the geometry of parallel transport. The internal stress representing the internal viscous stress has been derived from variational principles, using a Rayleigh potential. All the relevant physical quantities, such as strain rates and internal stress, have been identified in the discrete setting. Using a formal convergence argument, we have shown equivalence of the discrete equations with the classical smooth formulation. The method has been validated against reference solutions available for steady coiling. Demonstration examples in the non-steady case have been shown.

We would like to thank Neil Ribe for getting us interested into the fascinating dynamics of thin threads, and for sharing his continuation data which enabled us to validate our code.

Appendix A. Equivalence with the constitutive equations of Ribe

In a classical paper, Ribe analyzed the helical coiling of viscous jets falling on a plane [9]. In the frame rotating with the jet, the shape of the centerline is stationary. The equations for the shape of the jet are expressed as a set of non-linear ordinary differential equations with boundary conditions at both ends. This non-linear boundary value problem was solved by numerical continuation techniques, using the AUTO [78] software. These solutions, which corresponds to steady configurations, have been used to validate our dynamical code.

We show below that the constitutive laws derived by Ribe from the Stokes equations in 3D, are equivalent to our equations (65). However, the formalism used by Ribe is different from ours, and we then need to reword his analysis.

Ribe introduces an Eulerian twist-curvature vector $\underline{\pi}^E$ which satisfies an equation similar to our equation (28) for its Lagrangian variant $\underline{\pi}$, where the derivative is taken with respect to s instead of S , that is:

$$\frac{\partial \underline{d}_i'}{\partial s} = \underline{\pi}^E \times \underline{d}_i. \quad (\text{A.1})$$

The components of $\underline{\pi}^E$ are denoted

$$\underline{\pi}^E = \begin{bmatrix} \kappa_1 \\ \kappa_2 \\ \kappa_3 \end{bmatrix}, \quad (\text{A.2})$$

where the square brackets indicate a decomposition in the material frame $(\underline{d}_1, \underline{d}_2, \underline{d}_3)$, which is a ‘moving’ frame, *i. e.* this frame varies with the arc length parameter.

As in equation (30), the Eulerian kinematical twist τ^E and binormal curvature vector \underline{K}^E are obtained by a decomposition of the twist-curvature vector $\underline{\pi}^E$ into transverse and tangential components,

$$\tau^E = \kappa_3, \quad \underline{K}^E = \begin{bmatrix} \kappa_1 \\ \kappa_2 \\ 0 \end{bmatrix}. \quad (\text{A.3})$$

In the frame rotating with the coils, the material rotation $\underline{\omega}_R$ is written in a form similar to equation (27),

$$\underline{\omega}_R = \underline{t} \times \dot{\underline{t}}_R + \omega_3 \underline{d}_3,$$

where $\dot{\underline{t}}_R$ is the time derivative evaluated in the rotating frame. Since the shape of the thread is steady in this frame, we have

$$\dot{\underline{t}}_R = U \frac{\partial \underline{\omega}_R}{\partial s} = U \underline{\pi}^E \times \underline{t},$$

where $U = \underline{u}_R \cdot \underline{t}$ is the axial velocity of the fluid in the rotating frame. The expression for the material angular velocity can be obtained by combining the above equations,

$$\underline{\omega}_R = \begin{bmatrix} U \kappa_1 \\ U \kappa_2 \\ \omega_3 \end{bmatrix}. \quad (\text{A.4})$$

The material angular velocity in the laboratory frame follows from the composition of velocities, that is $\underline{\omega} = \underline{\omega}_R + \Omega \underline{e}_z$ where Ω is the frequency of coiling, as well as the relative angular velocity of the rotating frame with respect to the laboratory.

As a result, the gradient of rotation reads

$$\frac{\partial \underline{\omega}}{\partial s} = \frac{\partial}{\partial s} \begin{bmatrix} U \kappa_1 \\ U \kappa_2 \\ \omega_3 \end{bmatrix} = \begin{bmatrix} (U \kappa_1)' \\ (U \kappa_2)' \\ \omega_3' \end{bmatrix} + \underline{\pi}^E \times \begin{bmatrix} U \kappa_1 \\ U \kappa_2 \\ \omega_3 \end{bmatrix},$$

where the last term comes from the fact that the material frame is a moving frame, see equation (A.1).

With the help of equations (A.2) and (A.4), this vector reads

$$\frac{\partial \underline{\omega}}{\partial s} = \begin{bmatrix} (U \kappa_1)' + \kappa_2 (\omega_3 - U \kappa_3) \\ (U \kappa_2)' - \kappa_3 (\omega_3 - U \kappa_3) \\ \omega_3' \end{bmatrix}$$

When this vector is inserted into the constitutive law (65b), we obtain for the bending moment \underline{m} the same expressions as those derived by Ribe, who used a lubrication-type of approximation in the Stokes equations in 3D.

References

- [1] M. G. Forest, H. Zhou, Unsteady analyses of thermal glass fibre drawing processes, *European Journal of Applied Mathematics* 12 (2001) 479–496.
- [2] J. R. A. Pearson, *Mechanics of polymer processing*, Applied science publishers, New York, NY, USA, 1985.
- [3] E. Andreassen, E. Gunderson, E. L. Hinrichsen, H. P. Langtangen, A mathematical model for the melt spinning of polymer fibers, in: M. D. et al. (Ed.), *Numerical methods and software tools in industrial mathematics*, Birkhauser, Boston, 1997, pp. 195–212.
- [4] D. Shimozuru, Physical parameters governing the formation of hair and tears, *Bulletin of volcanology* 56 (3) (1994) 217–219.
- [5] A. Herczynski, C. Cernuschi, L. Mahadevan, Painting with drops, jets, and sheets, *Physics Today* 31 (31) (2011) 32–36.
- [6] G. Barnes, R. Woodcock, Liquid rope-coil effect, *American Journal of Physics* 26 (1958) 205–209.
- [7] G. I. Taylor, Instability of jets, threads, and sheets of viscous fluid, in: Springer (Ed.), *Proceedings of the 12th International Congress on Applied Mechanics*, Stanford, 1968, p. 382.
- [8] L. Mahadevan, W. S. Ryu, A. D. T. Samuel, Fluid ‘rope trick’ investigated, *Nature* 392 (140) (1998) 502.
- [9] N. M. Ribe, Coiling of viscous jets, *Proceedings of the Royal Society A: Mathematical, Physical and Engineering Sciences* 460 (2051) (2004) 3223–3239.
- [10] N. M. Ribe, H. E. Huppert, M. A. Hallworth, M. Habibi, D. Bonn, Multiple coexisting states of liquid rope coiling, *Journal of Fluid Mechanics* 555 (1) (2006) 275–297.
- [11] N. M. Ribe, M. Habibi, D. Bonn, Stability of liquid rope coiling, *Physics of Fluids* 18 (8) (2006) 084102.
- [12] S. Chiu-Webster, J. R. Lister, The fall of a viscous thread onto a moving surface: a ‘fluid-mechanical sewing machine’, *Journal of Fluid Mechanics* 569 (2006) 89–111.
- [13] S. W. Morris, J. H. P. Dawes, N. M. Ribe, J. R. Lister, Meandering instability of a viscous thread, *Physical Review E (Statistical, Nonlinear, and Soft Matter Physics)* 77 (6) (2008) 066218.
- [14] F. R. S. Trouton, On the coefficient of viscous traction and its relation to that of viscosity, *Proceedings of the Royal Society of London, A* 77 (1906) 426–440.

- [15] J. D. Buckmaster, A. Nachman, L. Ting, The buckling and stretching of a viscida, *Journal of Fluid Mechanics* 69 (01) (1975) 1–20.
- [16] C. W. Hirt, J. P. Shannon, Free-surface stress conditions for incompressible-flow calculations, *Journal of Computational Physics* 2 (1968) 403–441.
- [17] B. D. Nichols, C. W. Hirt, Improved free surface boundary conditions for numerical incompressible-flow calculations, *Journal of Computational Physics* 8 (1971) 434–448.
- [18] M. F. Tome, S. McKee, GENSMAC: A computational marker and cell method for free surface flows in general domains, *Journal of Computational Physics* 110 (1) (1994) 171–186.
- [19] M. F. Tome, S. McKee, Numerical simulation of visous flow: Buckling of planar jets, *Int. J. Numer. Meth. Fluids* 29 (1999) 705–718.
- [20] C. M. Oishi, M. F. Tomé, J. A. Cuminato, S. McKee, An implicit technique for solving 3D low reynolds number moving free surface flows, *Journal of Computational Physics* 227 (16) (2008) 7446–7468.
- [21] W. Arne, N. Marheineke, A. Meister, R. Wegener, Numerical analysis of Cosserat rod and string models for viscous jets in rotational spinning processes, *Mathematical Models and Methods in Applied Sciences* 11 (20).
- [22] N. Marheineke, R. Wegener, Asymptotic model for the dynamics of curved viscous fibres with surface tension, *Journal of Fluid Mechanics* 622 (2009) 345–369.
- [23] M. Skorobogatiy, L. Mahadevan, Folding of viscous sheets and filaments, *Europhysics Letters* 52 (5) (2000) 532–538.
- [24] N. M. Ribe, Periodic folding of viscous sheets, *Physical Review E (Statistical, Nonlinear, and Soft Matter Physics)* 68 (3) (2003) 036305.
- [25] M. J. Blount, J. R. Lister, The asymptotic structure of a slender dragged viscous thread, *Journal of Fluid Mechanics* 674 (2011) 489–521.
- [26] M. Habibi, Y. Rahmani, D. Bonn, N. M. Ribe, Buckling of liquid columns, *Physical Review Letters* 104 (2010) 074301.
- [27] M. Habibi, P. C. F. Møller, N. M. Ribe, D. Bonn, Spontaneous generation of spiral waves by a hydrodynamic instability, *Europhysics Letters* 81 (2008) 38004.
- [28] J. H. Maddocks, D. J. Dichmann, Conservation laws in the dynamics of rods, *Journal of elasticity* 34 (1994) 83–96.
- [29] A. Goriely, M. Tabor, New amplitude equations for thin elastic rods, *Phys. Rev. Lett.* 77 (17) (1996) 3537–3540.

- [30] A. Goriely, M. Tabor, Nonlinear dynamics of filaments II. nonlinear analysis, *Physica D: Nonlinear Phenomena* 105 (1-3) (1997) 45–61.
- [31] N. Clauvelin, B. Audoly, S. Neukirch, Matched asymptotic expansions for twisted elastic knots: a self-contact problem with non-trivial contact topology, *Journal of the Mechanics and Physics of Solids* 57 (2009) 1623–1656.
- [32] T. Y. Hou, I. Klapper, H. Si, Removing the stiffness of curvature in computing 3-D filaments, *Journal of Computational Physics* 143 (2) (1998) 628–664.
- [33] H. Weiss, Dynamics of geometrically nonlinear rods: II - numerical methods and computational examples, *Nonlinear dynamics* 30 (2002) 383–415.
- [34] S. Goyal, N. C. Perkins, C. L. Lee, Nonlinear dynamics and loop formation in Kirchhoff rods with implications to the mechanics of DNA and cables, *Journal of Computational Physics* 209 (1) (2005) 371–389.
- [35] M. Bergou, M. Wardetzky, S. Robinson, B. Audoly, E. Grinspun, Discrete elastic rods, *ACM Transactions on Graphics* 27 (3) (2008) 63.
- [36] S. Lim, A. Ferent, X. S. Wang, C. S. Peskin, Dynamics of a closed rod with twist and bend in fluid, *SIAM Journal on Scientific Computing* 31 (1) (2008) 273–302.
- [37] P. Jung, S. Leyendecker, J. Linn, M. Ortiz, A discrete mechanics approach to Cosserat rod theory. part 1: static equilibria, *International Journal for Numerical Methods in Engineering*.
- [38] T. B. Benjamin, T. Mullin, Buckling instabilities in layers of viscous liquid subjected to shearing, *Journal of Fluid Mechanics* 195 (1988) 523–540.
- [39] R. da Silveira, S. Chaïeb, L. Mahadevan, Rippling instability of a collapsing bubble, *Science* 287.
- [40] R. Radovitzky, M. Ortiz, Error estimation and adaptative meshing in strongly nonlinear dynamic problems, *Computer Methods in Applied Mechanics and Engineering* 172 (1999) 203–240.
- [41] M. Bergou, B. Audoly, E. Vouga, M. Wardetzky, E. Grinspun, Discrete viscous threads, *Transactions on Graphics* 29 (4) (2010) 116.
- [42] V. M. Entov, A. L. Yarin, The dynamics of thin liquid jets in air, *J. Fluid Mech.* 140 (1984) 91–111.
- [43] J. Buckmaster, The buckling of thin viscous jets, *Journal of Fluid Mechanics* 61 (3) (1973) 449–463.
- [44] J. D. Buckmaster, A. Nachman, The buckling and stretching of a viscida II. Effects of surface tension, *The Quarterly Journal of Mechanics and Applied Mathematics* 31 (2) (1978) 157–168.

- [45] J. N. Dewynne, J. R. Ockendon, P. Wilmot, A systematic derivation of the leading-order equations for extensional flows in slender geometries, *Journal of Fluid Mechanics* 24 (1992) 323–338.
- [46] L. J. Cummings, P. D. Howell, On the evolution of non-axisymmetric viscous fibres with surface tension, inertia and gravity, *Journal of Fluid Mechanics* 389 (1999) 361–389.
- [47] S. Panda, N. Marheineke, R. Wegener, Systematic derivation of an asymptotic model for the dynamics of curved viscous fibers, *Mathematical Methods in the Applied Sciences* 31 (10) (2008) 1153–1173.
- [48] S. E. Bechtel, M. G. Forest, D. B. Bogy, A one-dimensional theory for viscoelastic fluid jets, with application to extrudate swell and draw-down under gravity, *Journal of Non-Newtonian Fluid Mechanics* 21 (3) (1986) 273–308.
- [49] S. E. Bechtel, J. Z. Cao, M. G. Forest, Practical application of a higher order perturbation theory for slender viscoelastic jets and fibers, *Journal of Non-Newtonian Fluid Mechanics* 41 (3) (1992) 201–273.
- [50] I. M. Griffiths, P. D. Howell, Mathematical modelling of non-axisymmetric capillary tube drawing, *Journal of Fluid Mechanics* 605 (2008) 181–206.
- [51] Q.-S. Nguyen, *Stability and nonlinear solid mechanics*, John Wiley & Sons Ltd, 2000.
- [52] R. Bishop, There is more than one way to frame a curve, *The American Mathematical Monthly* 83 (1975) 246–251.
- [53] J. Langer, D. A. Singer, Lagrangian aspects of the Kirchhoff elastic rod, *SIAM Review* 38 (4) (1996) 605–618.
- [54] R. E. Goldstein, T. R. Powers, C. H. Wiggins, Viscous nonlinear dynamics of twist and writhe, *Phys. Rev. Lett.* 80 (23) (1998) 5232–5235.
- [55] F. Boyer, D. Primault, Finite element of slender beams in finite transformations: a geometrically exact approach, *International Journal for Numerical Methods in Engineering* 59 (5) (2004) 669–702.
- [56] B. Audoly, Y. Pomeau, *Elasticity and geometry: from hair curls to the nonlinear response of shells*, Oxford University Press, 2010.
- [57] G. Călugăreanu, L’intégrale de Gauss et l’analyse des nœuds tridimensionnels, *Revue de mathématiques pures et appliquées* 4 (5) (1959) 5–20.
- [58] W. Pohl, The self-linking number of a closed space curve, *Indiana University Mathematics Journal* 17 (1968) 975–985.
- [59] J. H. White, Self-linking and the Gauss integral in higher dimensions, *American Journal of Mathematics* 91 (3) (1969) 693–728.

- [60] F. B. Fuller, The writhing number of a space curve, PNAS 68 (4) (1971) 815–819.
- [61] F. B. Fuller, Decomposition of the linking number of a closed ribbon: a problem from molecular biology, PNAS 75 (8) (1978) 3557–3561.
- [62] J. Aldinger, I. Klapper, M. Tabor, Formulae for the calculation and estimation of writhe, Journal of Knot Theory and Its Ramification 4 (3) (1995) 343–372.
- [63] F. Tanaka, H. Takahashi, Elastic theory of supercoiled DNA, Journal of Chemical Physics 83 (11) (1985) 6017.
- [64] J. H. White, W. R. Bauer, Calculation of the twist and the writhe for representative models of dna, Journal of Molecular Biology 189 (2) (1986) 329–341. doi:10.1016/0022-2836(86)90513-9.
- [65] I. Tobias, B. D. Coleman, W. K. Olson, The dependence of DNA tertiary structure on end conditions: Theory and implications for topological transitions, The Journal of Chemical Physics 101 (12) (1994) 10990–10996.
- [66] K. Klenin, J. Langowski, Computation of writhe in modeling of supercoiled DNA, Biopolymers 54 (5) (2000) 307–317.
- [67] A. C. Maggs, Writhing geometry at finite temperature: Random walks and geometric phases for stiff polymers, The Journal of Chemical Physics 114 (13) (2001) 5888–5896. doi:10.1063/1.1353545.
- [68] C. W. Wolgemuth, T. R. Powers, R. E. Goldstein, Twirling and whirling: Viscous dynamics of rotating elastic filaments, Phys. Rev. Lett. 84 (7) (2000) 1623–1626.
- [69] M. Levitt, Protein folding by restrained energy minimization and molecular dynamics, Journal of Molecular Biology 170 (3) (1983) 723–764.
- [70] B. Torby, Advanced Dynamics for Engineers, HRW series in mechanical engineering, Holt Rinehart and Winston, 1984.
- [71] A. L. Yarin, Free Liquid Jets and Films: Hydrodynamics and Rheology, Longman, New York, New York, 1993.
- [72] C. Batty, R. Bridson, Accurate viscous free surfaces for buckling, coiling, and rotating liquids, in: Proceedings of the 2008 ACM/Eurographics Symposium on Computer Animation, 2008, pp. 219–228.
- [73] R. M. Wald, General relativity, University of Chicago Press, 1984.
- [74] R. de Vries, Evaluating changes of writhe in computer simulations of supercoiled DNA, The Journal of Chemical Physics 122 (2005) 064905.

- [75] E. Hairer, C. Lubich, G. Wanner, Geometric Numerical Integration, 2nd Edition, Vol. 31 of Springer Series in Computational Mathematics, Springer, 2006.
- [76] P.-T. Brun, N. M. Ribe, B. Audoly, A numerical investigation of the fluid mechanical sewing machine, to appear in *Physics of fluids* (2012).
- [77] M. A. Otaduy, R. Tamstorf, D. Steinemann, M. Gross, Implicit contact handling for deformable objects, *Computer Graphics Forum* 28 (2) (2009) 559–568.
- [78] E. Doedel, A. R. Champneys, T. F. Fairgrieve, Y. A. Kuznetsov, B. Sandstede, X. J. Wang, AUTO97: continuation and bifurcation software for ordinary differential equations, Available at <http://indy.cs.concordia.ca/auto/> (2002).
- [79] H. Tabuteau, S. Mora, G. Porte, M. Abkarian, C. Ligoure, Microscopic mechanisms of the brittleness of viscoelastic fluids, *Physical Review Letters* 102 (15) (2009) 155501.
- [80] T. S. Majmudar, M. Varagnat, W. Hartt, G. H. McKinley, Nonlinear dynamics of coiling in viscoelastic jets, preprint arXiv:1012.2135v1 (2010).
- [81] A. Bonito, M. Picasso, M. Laso, Numerical simulation of 3D viscoelastic flows with free surfaces, *Journal of Computational Physics* 215 (2) (2006) 691–716.
- [82] A. Rafiee, M. T. Manzari, M. Hosseini, An incompressible SPH method for simulation of unsteady viscoelastic free-surface flows, *International Journal of Non-Linear Mechanics* 42 (10) (2007) 1210–1223.